Delft University of Technology

Effect of natural carbonation on the pore structure and elastic modulus of the alkali-activated fly ash and slag pastes

Nedeljkovic, M.; Savija, B.; Zuo, Yibing; Luković, Mladena; Ye, Guang

Important note
To cite this publication, please use the final published version (if applicable).
Please check the document version above.

Effect of natural carbonation on the pore structure and elastic modulus of the alkali-activated fly ash and slag pastes

Marija Nedeljković[a*], Branko Šavija[a,b], Yibing Zuo[a], Mladena Luković[c], Guang Ye[a,d]

[a] Microlab, Faculty of Civil Engineering and Geosciences, Delft University of Technology, Stevinweg 1, 2628 CN Delft, The Netherlands

[b] TNO Technical Sciences, Structural Reliability, Delft, The Netherlands

[c] Concrete Structures, Faculty of Civil Engineering and Geosciences, Delft University of Technology, Stevinweg 1, 2628 CN Delft, The Netherlands

[d] Magnel Laboratory for Concrete Research, Department of Structural Engineering, Ghent University Technologiepark-Zwijnaarde 904 B-9052, Ghent (Zwijnaarde), Belgium

e-mail: M.Nedeljkovic@tudelft.nl
B.Savija@tudelft.nl
Y.Zuo@tudelft.nl
M.Lukovic@tudelft.nl
G.Ye@tudelft.nl

[*] Corresponding author
Tel: +31(0)15 27 82290

ABSTRACT

The aim of this paper was to investigate the effect of natural carbonation on the pore structure, and elastic modulus (E_m) of alkali-activated fly ash (FA) and ground granulated blast furnace slag (GBFS) pastes after one year of exposure in the natural laboratory conditions. The chemical changes due to carbonation were examined by X-ray diffraction (XRD), scanning electron microscope/energy-dispersive X-ray (SEM-EDX) and attenuated total reflectance Fourier transformed infrared spectroscopy (ATR-FTIR). Subsequently, the pore structure and E_m of the degraded material were tested by mercury intrusion porosimetry (MIP), nitrogen (N_2) adsorption, and nanoindentation.

1   The chemical degradation of alkali-activated pastes due to natural carbonation is

2 showed to be dependent on the GBFS content and their pore structure development. It was

3 found that the pure alkali-activated GBFS paste was not carbonated at all within the tested

4 period due to fine gel pore structure. On the other hand, carbonation of the gel in the pastes

5 consisting FA and GBFS generated significant mineralogical and microstructural changes.

6 The extensive decalcification of the gel was reflected in the increase of nanoporosity.

7 Consequently, the E_m of the carbonated pastes decreased.

8   This study suggests that the degradation of alkali-activated FA and GBFS pastes due

9 to carbonation may be accurately evaluated through micromechanical properties

10 measurements rather than only by testing alkalinity of the pore solution and corrosion of

11 reinforcement such as commonly studied carbonation effect in the ordinary Portland cement

12 (OPC)-based materials.

13 **Keywords:** Alkali-activated FA/GBFS, Natural carbonation, Pore structure, Nanoindentation,

14 E_m

15

16

17

18

19

20

21

22

23

1. Introduction

Alkali-activated materials (AAM), as environmentally friendly alternatives to OPC-based materials due to their comparatively low CO_2 emission and low natural resources consumption, have received much attention in the last twenty years [1, 2]. AAM can be produced from mixing different industrial by-products, such as FA, GBFS, bottom ash, waste glass, agricultural waste etc. with appropriate alkaline solutions [3]. In comparison with OPC-based materials, AAM might have better mechanical properties, stronger interfacial transition zone (ITZ), and better fire and chemical resistance [4]. However, the long-term properties of AAM, specifically carbonation resistance, are still unknown, which limits their application in engineering practice [5, 6].

In general, the CO_2 gas reaction-diffusion process in porous media is controlled by both the concentration gradient of CO_2 and the rate of the chemical reaction. Carbonation rate and degree in OPC-based materials and AAM depends on their physical and chemical properties and exposure conditions (i.e. relative humidity (RH), CO_2 concentration, temperature, duration of exposure). However, OPC-based materials and AAM exhibits different mechanisms during carbonation [7-10], due to formation and interaction of different phases in these two systems. While portlandite ($Ca(OH)_2$) and calcium silicate hydrate gel (C-S-H) are the primary sources of Ca^{2+} ions in the carbonation process of OPC-based materials [11], the alkali calcium aluminate silicate hydrate gel, denoted further in the text as a C-(N-)A-S-H gel, similar to [12], is the main source of Ca^{2+} ions for carbonation reactions in GBFS-based or different blended AAM (GBFS, FA, metakaolin). The removal of the calcium ions from the gel interlayers and gel sheet layers during carbonation induces shrinkage due to the molecular structural reorganization of the gels. This reaction is followed by a decrease in the volume of the paste, which is called carbonation shrinkage [13].

1   Depending on the binder composition, the effect of carbonation on the mechanical

2   properties can vary. Mechanical properties of OPC pastes can be considerably improved by

3   carbonation [14, 15], because carbonation of the $Ca(OH)_2$ leads to a reduction in porosity due

4   to the positive difference of molar volumes between $Ca(OH)_2$ and $CaCO_3$. Measured by

5   nanoindentation, hardness and elastic modulus tend to shift to higher values in the OPC paste.

6   On the other hand, micro-mechanical properties of blended OPC and GBFS (such as CEM III-

7   B) pastes decrease due to carbonation, since they contain less $Ca(OH)_2$ and have a lower

8   Ca/Si ratio in the C-S-H gel [16, 17]. It has been found that at extensive levels of

9   decalcification (when Ca/Si is below ~0.66), decomposition of the Ca-O sheets of the C-S-H

10   leads to significant shrinkage due to precipitation of calcium carbonates and subsequent

11   polymerization of the silica gel [18], resulting in decrease of the mechanical strength.

12   Only a few studies so far have discussed mechanical behavior of carbonated AAM.

13   For instance, Bakharev et al. [7] found that the carbonation resistance of alkali-activated slag

14   (AAS) concrete was lower than that of OPC concrete. The AAS concrete had higher strength

15   loss and carbonation depth than OPC concrete in both investigated exposure conditions, i.e.

16   immersion in 0.352 molar (M) sodium bicarbonate solution, and exposure to atmosphere with

17   10–20% of CO_2 at 70% RH. Nevertheless, both sets of the conditions are highly aggressive

18   and the results cannot be directly used to predict in-service behavior of AAS concrete

19   subjected to natural carbonation.

20   Bernal et al. investigated accelerated carbonation of alkali silicate-activated GBFS

21   mortars, under the condition of CO_2 concentration of 3.0±0.2%, temperature of 20±2 °C, and

22   65±5% RH [19]. Noncarbonated specimens had compressive strengths of up to 63 MPa after

23   28 days of curing when granulated GBFS was used as the sole binder. The strength decreased

24   by 40-50% after carbonation.

1   Puertas et al. [9] studied the effect of alkaline activator on carbonation degree in AAS

2   mortars in terms of mechanical properties. When sodium waterglass was used as an activator,

3   decalcification of the C-S-H gel prompted by carbonation led to a loss of cohesion in the

4   matrix, increase in porosity, and the reduction of the compressive strength. On the other hand,

5   when NaOH was used as activator, carbonation enhanced the compressive strength of the

6   mortar. The authors assumed that this was due to the precipitation of calcium carbonates in

7   the pores, causing a decline in the total porosity and average pore size.

8   Since effect of carbonation in the previous studies was mainly investigated on bulk

9   macro-mechanical properties of alkali-activated mortars or concretes, it is difficult to

10   understand its effects on the local micro-mechanical properties of the binder. Several

11   parameters can affect the interpretation of the mechanical behavior of the material due to the

12   carbonation if they are studied at concrete (macro) level and not at the paste (micro) level.

13   The most important are:

14   •   Effect of the material scale: Pastes are more suitable for the analysis due to their

15   homogeneity, compared to concrete. The presence of aggregates in the concrete

16   encompasses paste aggregate interface, which can carbonate faster due to its higher

17   porosity compared to the paste itself. Therefore, the carbonation study on the paste

18   samples is needed first for understanding of more complex carbonation mechanism at

19   the concrete scale.

20   •   Effect of the sample size: Carbonation reaction is dominant at the concrete surface

21   and in the first several millimeter depth from the surface. Therefore, effects of

22   measuring the bulk mechanical properties (compressive, tensile or flexural strength)

23   will be largely dependent on the size of the sample. For instance, the standard

24   150x150x150 mm^3 concrete cubes NEN [5988:1999] will be useless in evaluation of

25   the natural carbonation effect on the compressive strength if the carbonated depth is

only a few millimeter. On the other hand, the coupled effects of different mechanisms at the concrete surface (e.g. drying shrinkage that can lead to cracking) and not only carbonation can overestimate the effect of the carbonation on the material properties.

- Effect of the testing scale (local/bulk): Testing of the local micromechanical properties provides a more reliable evaluation on chemical degradation of the paste, compared to a bulk test such as the compressive strength test of a standard concrete cube. With a local analysis the chemical degradation of the different phases present in the system can be distinguished and correlated with the chemical analysis. Furthermore, on the same sample, testing of both, carbonated and noncarbonated areas is possible.

Considering these effects, it is clear that understanding the influence of carbonation on the micro-mechanical properties at the paste level is the first step towards understanding the properties of carbonated concrete. Therefore, assessment of the micro-mechanical properties is needed, such as E_m, which might be of great importance for predicting the service life and degradation degree of AAM.

The aim of this study was to evaluate the effect of chemical changes in the alkali-activated FA and GBFS pastes when exposed in the natural laboratory conditions (~55% RH, ~0.038% CO_2 v/v) on the pore structure and E_m. The gel structural changes were investigated by XRD, SEM-EDX and ATR-FTIR, while MIP, N_2 adsorption, and nanoindentation were used to examine pore structure and E_m after carbonation.

## 2. Materials and methods

2.1. Materials and sample preparation

The precursors used in this study were FA from VLIEGASUNIE BV and GBFS from ORCEM (the Netherlands), with chemical compositions as shown in Table 1. The main crystalline phases in FA were quartz, mullite, and hematite, while GBFS was mainly

1 amorphous, as showed by XRD scans (Fig. 1). The alkaline activator was synthetized by

2 mixing anhydrous pellets of sodium hydroxide with deionized water and commercial sodium

3 silicate solution (27.5 wt.% SiO_2, 8.25 wt.% Na_2O). The activator concentration was 4.8 wt.%

4 Na_2O with respect to the mass of precursor (FA + GBFS). After mixing, the activator was

5 kept in the laboratory with temperature around 20°C to cool down for 24 h prior to the

6 preparation of the pastes. For each paste, the liquid to binder mass ratio was 0.5. Pastes were

7 produced with the following FA/GBFS ratios: 100:0, 70:30, 50:50, 30:70, 0:100 wt.%, named

8 S0, S30, S50, S70, S100, respectively. The precursors were dry-mixed for 2 minutes and then

9 mixed with the activator. The pastes exposed to carbonation were cast in cylinders with 54

10 mm diameter and height of 100 mm. The samples were placed in a fog room with 20°C and

11 99 % RH and cured under sealed conditions for 28 days. After 28 days, the samples were

12 demolded and exposed in the indoor laboratory conditions at 20°C and 55 % RH,

13 CO_2~0.038% v/v for 1 year. In addition, reference samples were kept in sealed conditions (i.e.

14 without CO_2) until the characterization was carried out. The representative samples prior to

15 microscopic examination are shown in Fig. 2. The carbonation depth was determined by

16 polarized light microscope (PLM) under cross polarized light as demonstrated in previous

17 study [20]. The carbonation depth values are presented in the Fig. 3.

18 **Table 1**

19 Chemical compositions of FA and GBFS measured by X-ray fluorescence.

|	SiO_2	Al_2O_3	CaO	MgO	Fe_2O_3	SO_3	Na_2O	K_2O	TiO_2	P_2O_5	L.O.I.
FA	54.28	23.32	4.23	1.62	8.01	0.64	0.85	1.97	1.23	0.54	3.37
GBFS	34.40	11.53	39.17	7.81	1.42	1.6	0.23	0.58	-	-	1.15
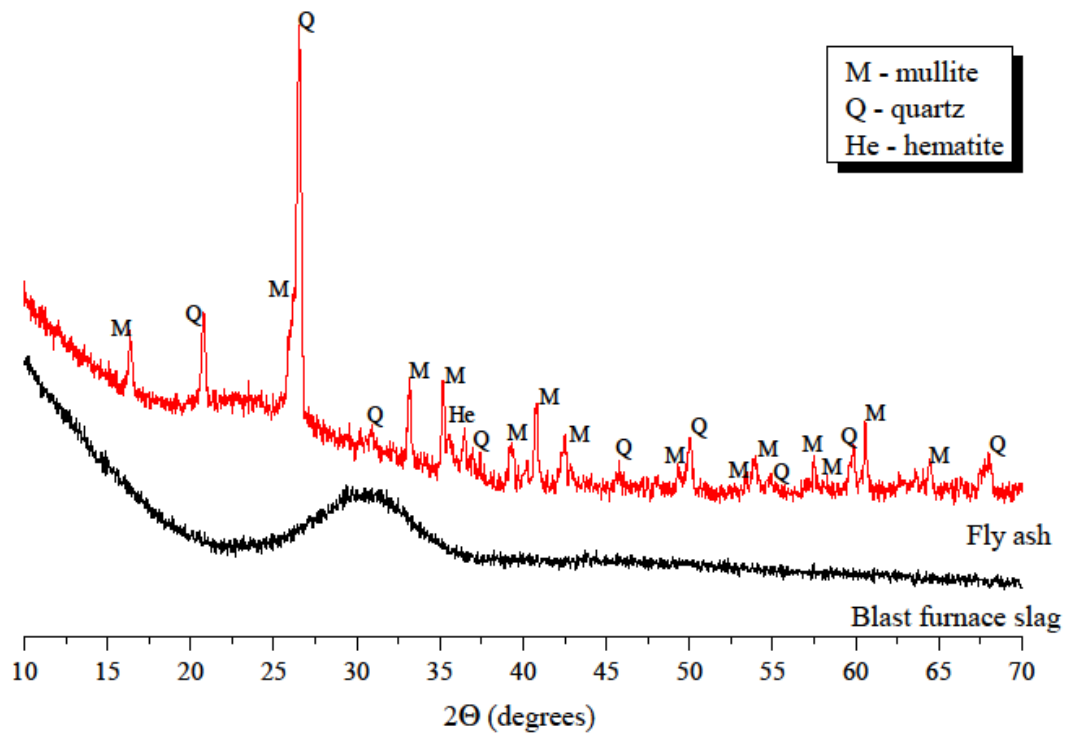
1

2 **Fig. 1.** XRD scans of original FA and GBFS.

3

4 **Fig. 2.** Cross-sections of representative samples after natural laboratory carbonation of 1 year,

5 clearly showing the outer (carbonated) and the inner (noncarbonated) zone. Reference

6 samples are of smaller diameter, placed beneath the exposed samples.

1
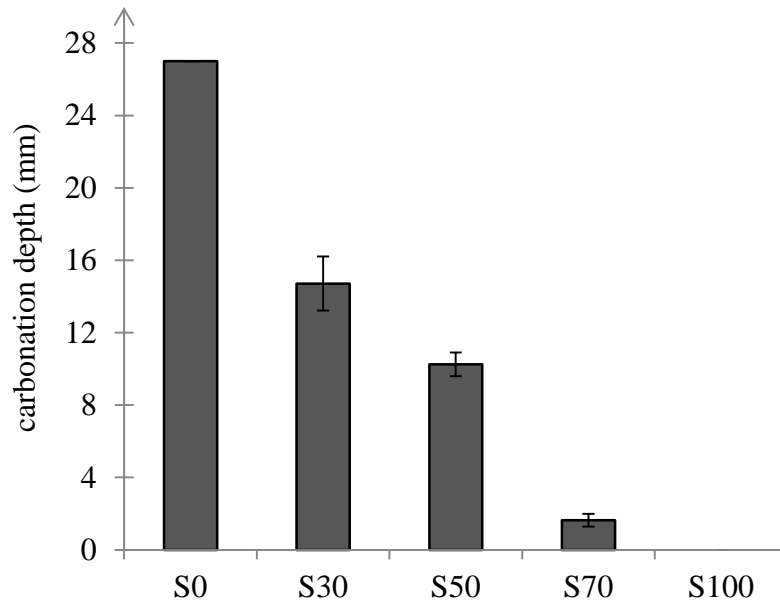
Fig. 3. Carbonation depth after 1 year exposure in the natural laboratory conditions, determined by PLM in the alkali-activated pastes as a function of the slag content.

2.2. Test methods

2.2.1 XRD

For XRD phase identification, the representative samples after 1 year of curing, and 1 year of exposure were gently crushed and then immersed in isopropanol for one week, by which water is first replaced and then evaporated. Subsequently, samples were placed under vacuum at 25 °C for minimum three weeks. In order to calculate the absolute phase weight proportions, the standard was homogeneously mixed with the sample. A few grams of hydration-stopped samples, were ground in a McCRONE micronizing mill to below 15 μm, with an internal standard. The known amount (10 wt.%) of internal standard which in this study was silicon (Si) has been used. XRD scans were acquired from 5° to 70° 2-theta with a Bruker D4 diffractometer using Co–Kα radiation and a Vantec detector. The identified phases were added to the Rietveld refinement. The software package Topas was used to perform Rietveld quantification of phases in the reference and exposed samples. Regarding precision

obtained on the content of the amorphous phase in the samples, the calculation showed high-precision results, with errors generally less than 1.0% absolute.

2.2.2 SEM-EDX

For SEM-EDX sample preparation, the hydration of the samples was stopped in the same way as for XRD analysis, whereas instead of grinding the samples into a powder, the reference and exposed samples (crushed into small pieces with dimensions of 1-2 cm^3) were impregnated using a low viscosity epoxy resin and polished down to ¼ μm.

To study the microstructure a Philips-XL30-ESEM was used, equipped with NSS.3.3 software. This instrument was used in normal high-vacuum mode as a regular SEM. In order to determine optimal microscope condition for microstructure analysis, the interaction volume was modelled using Monte Carlo simulation in Casino v2.41 software (www.gel.usherbrooke.ca/casino/index.html) for unreacted GBFS and for the C-(N-)A-S-H gel that is formed in alkali-activated GBFS [12] (Fig. 4), using their experimental density (2.9 g/cm^3 for GBFS and 2.6 g/cm^3 C-(N-)A-S-H gel) as an input parameter. First, the multiple energies were simulated (not shown here) from 5 to 20 kV with a step of 5, in order to demonstrate the effect of the accelerated voltage on the depth and the width of the electrons-solid material interaction. Fig. 4 demonstrates the depth of the electrons-solid material interaction, while using 15 kV for the simulation, which was chosen as an optimum in this study for experiments from previous iterative study. It was found that the maximum penetration depth of the electron trajectories ranges from 0.6 to 1.8 μm for GBFS particles and from 1.0 to 2.5 μm for C-(N-)A-S-H gel at 15 kV (Fig. 4). For backscattered electrons, the maximum sampling depth is about 30% of the interaction volume depth and its lateral dimension is close to the interaction volume depth. As electrons penetrate deeper, the lateral

1 spread of the electron-solid interaction region increases. The lateral dimension of the

2 interaction volume for cement-based materials is thought to be around 1-2 μm [21].

3

4
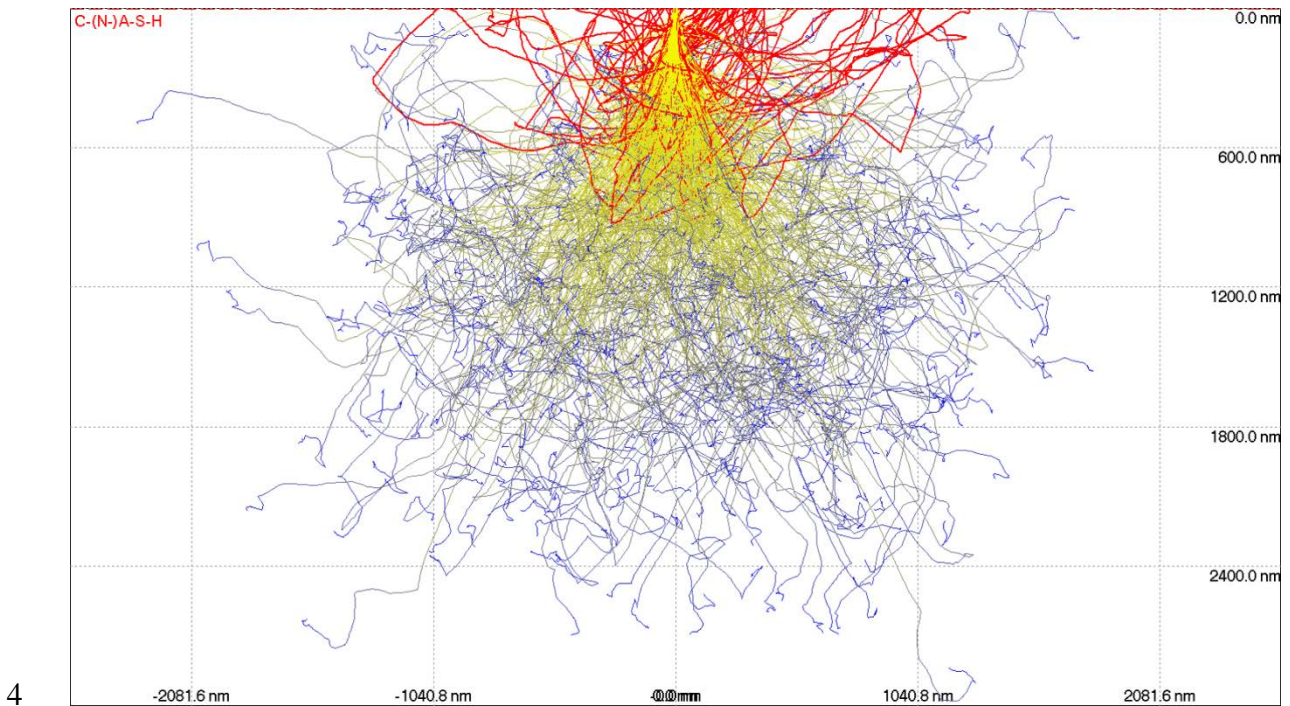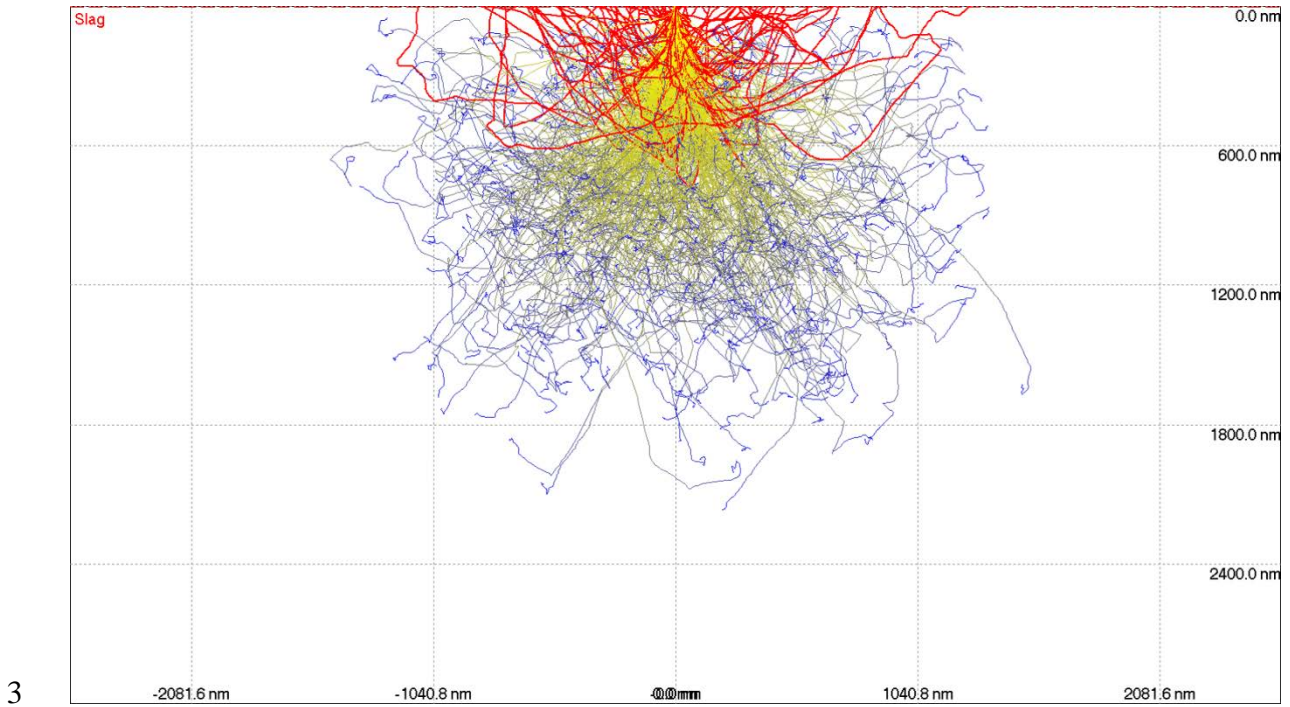
5 **Fig. 4.** Monte Carlo simulation of the penetration of 1000 electrons accelerated at 15kV in a

6 beam of radius 10 nm into a GBFS (upper image) and C-(N-)A-S-H gel (bottom image). (The

7 red trajectories are back-scattered electrons, which result from elastic scattering events.

Inelastic scattering events cause a reduction of energy of the electrons until eventual disappearance in the specimen bulk. Yellow trajectories represents high energy and blue represents low energy trajectories.)

For chemical compositions of the reaction products, SEM-EDX point analyses were used. Carbon coating was applied to the polished sections of the samples. Approximately 30 points were captured and analysed in each carbonated and noncarbonated gel area per sample. The mean atomic ratios for Na/Si, Mg/Si, Ca/Si, Al/Si were then obtained by averaging the values from more than 30 points. The points were chosen combining SEM-EDX at magnification sufficient to resolve carbonation features. Before and after each spot measurement, corrections were applied using ZAF method. The ZAF method is aimed to convert apparent concentrations (raw peak intensity) into (semi-quantitative) concentrations corrected for inter-element matrix effects. The ZAF method is iterative and in order to proceed it needs information on concentrations. However, these are absent at the beginning. Thus the results from the first iteration are fed back to the second and so on until a limit is reached that is statistically satisfactory.

2.2.3   ATR-FTIR

The chemical bonds of the powdered reference and carbonated samples were characterized by ATR-FTIR. Spectra were acquired using PerkinElmer Spectrum 100, over the wavelength range of 2000 cm^{-1} to 600 cm^{-1} with a resolution of 4 cm^{-1}. In total, 16 scans were collected per measurement. Samples were prepared in the same manner as for XRD measurements.

2.2.4   MIP and N_2

1   Porosity and pore-size distribution were investigated by MIP measurements combined

2   with N_2 adsorption, following the sample preparation procedure as described for XRD

3   analysis, with exception that samples were not ground. MIP measurements were performed

4   with Micrometrics PoreSizer® 9320. The PoreSizer® 9320 is a 207-MPa mercury intrusion

5   porosimeter, which determines pore sizes in the range of 7 nm to 500 µm. The threshold pore

6   size was obtained from the intersection of the two tangents in the intrusion curve, such as

7   showed in [21], using Washburn's equation, with a contact angle of 140° and a surface tension

8   of 0.485 N/m [22]. The pore size distribution in the range of 2-37 nm were determined by N_2

9   adsorption. The N_2 adsorption tests were conducted by using Gemini VII 2390 with a relative

10   pressure (P/P_0) range from 0.05~0.99 (the relative pressure is defined as the equilibrium vapor

11   pressure divided by the saturation vapor pressure). Approximately 1 gram of sample was used

12   for the analysis. According to N_2 adsorption isotherm the pore volume and area distribution

13   were calculated by the Barrett-Joyner-Halenda (BJH) method [23]. The sharp peaks that were

14   found in the pore size distributions curves, corresponding to the threshold (critical) pore

15   diameter, were determined according to [24].

16   2.2.5   Nanoindentation
17

18   Nanoindentation is a widely used technique for testing nano or micro-mechanical

19   properties of cementitious materials [25-29], and also of AAM [30-34]. For heterogeneous

20   multiphase materials, a statistical indentation method can be used, by analyzing a large

21   number of indents within a representative sample area [35, 36]. It consists of indenting a

22   sample surface with a diamond indenter, followed by a loading-unloading cycle while

23   continuously recording the load and indentation depth. From the load-displacement slope and

24   calibrated contact area, E_m of the material at the microscale can be determined.

1   Nanoindentation testing was conducted using Agilent Nano Indenter G200, equipped

2   with a Berkovich indenter. Nanoindentation was used to examine E_m, for carbonated and

3   noncarbonated areas. The samples for nanoindentation testing were first cut into slices of

4   approximately 10 mm thickness. Then they were ground and polished following the procedure

5   described in Table 2, to obtain a very flat and smooth ("mirror-like") surface. The tests were

6   set in such a way that the loading was applied when the indenter comes into the contact with

7   the surface of the sample until a specified maximum penetration depth is reached. Afterwards,

8   the load was maintained for 10 seconds followed by the unloading cycle. A typical example

9   of an indentation curve is shown in Fig. 6. The indentation depth was 2000 nm. This depth

10 was chosen because the scale of SEM-EDX analysis was ~2000 nm, which allows the

11 correlation between chemical and micro-mechanical results, as reported by Ulm et al. [37,

12 38].

13   The measurements were performed on the top surface of the specimens. The E_m

14 measurements were obtained from a matrix of 15x15 indents, with a distance of 40 μm

15 between individual indents. The indentation mesh for the noncarbonated S50 sample is

16 visualized in Fig. 5.

17   The Continuous Stiffness Method developed by Oliver and Pharr [39] was used to

18 calculate the reduced modulus of elasticity (E_r), according to Eq. (1):

$$E_r = \frac{\sqrt{\pi}}{2}\frac{S}{\sqrt{A_c}} \quad (1)$$

19 where S is the contact stiffness determined from the load-indentation depth slope, and A_c is

20 the contact area under load (μm^2), which is the function of the indentation depth. Since the

21 effect of non-rigid indenter also must be taken in account, the modulus of elasticity of the

22 sample, E_s (GPa) is calculated from the Eq. (2):

$$\frac{1}{E_r} = \frac{(1-v_s)^2}{E_s} + \frac{(1-v_i)^2}{E_i} \quad (2)$$

1 where v_s is the Poisson's ratio of the sample, which was assumed to be 0.18 for all

2 measurements. E_i is the modulus of elasticity of the diamond indenter, and v_i is the Poisson's

3 ratio of the diamond indenter (E_i = 1141 GPa, v_i = 0.07).

4 This method enables that E_m is obtained as a continuous function of the indentation depth.

5 Therefore, for each indent, the average E_m was determined in the loading range between 1000

6 and 1800 nm depth.

7

8 **Table 2**

9 Polishing procedure of the samples adopted in this study for SEM-EDX and Nanoindentation

10 measurements.

| Sandpaper	Grit (µm)	Methods	Duration (min)
P-grade 120	125	With ethanol	5
P-grade 320	46.2	With ethanol	5
P-grade 500	30.2	With ethanol	5
P-grade 800	25.8	With ethanol	5
P-grade 1200	15.3	With ethanol	5
Diamond paste	6	Ultrasonic bath with ethanol, air gun dry	5
Diamond paste	3	Ultrasonic bath with ethanol, air gun dry	5
Diamond paste	1	Ultrasonic bath with ethanol, air gun dry	5
Diamond paste	0.25	Ultrasonic bath with ethanol, air gun dry	5

11
12
13
14
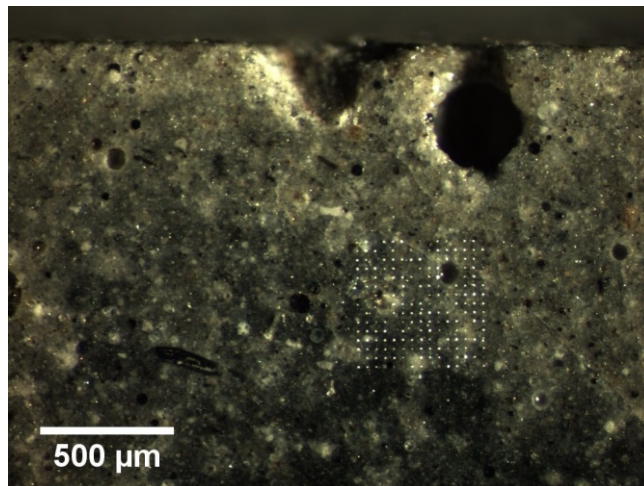
Fig. 5. Light microscope photo of the area of indents in noncarbonated S50 sample.
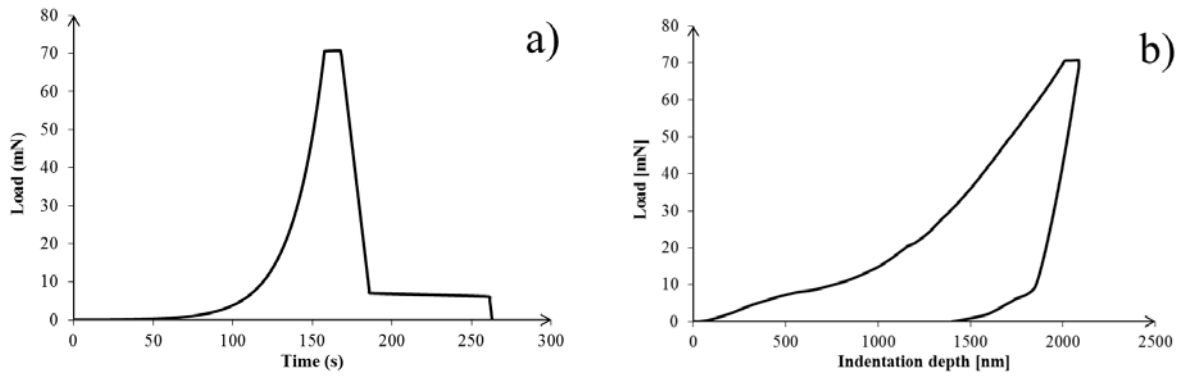
Fig. 6. Example of (a) load-time and (b) load-indentation depth curves by nanoindentation.

1

2 **3. Results and discussion**

3   In this section, results are presented in five subsections. First, the characterization of

4 the carbonation products is shown using XRD. Next, the spectroscopic analysis of the

5 carbonated and noncarbonated gel structure is demonstrated by SEM-EDX and ATR-FTIR.

6 Subsequently, the pore structure measurements of the carbonated and noncarbonated paste are

7 discussed. The last subsection shows the effect of carbonation on the elastic modulus, which

8 was significantly affected by the GBFS content.

9   3.1.   Mineralogical alteration by XRD

10   The aim of XRD analysis was to clearly differentiate carbonation products. Fig. 7

11 shows an example of the qualitative analysis of the reference and carbonated S50 samples.

12 The major phases for reference S50 sample, were amorphous phase (consisted of unreacted

13 amorphous phase and reaction phases, i.e. amorphous gel), and crystalline phases such as

14 quartz (SiO_2), mullite ($Al_{4.75}Si_{1.25}O_{9.63}$), hematite ($Fe_2O_3$), magnetite ($Fe_3O_4$), and traces of

15 calcite ($CaCO_3$). The identified crystalline phases stem from the original mineralogical

16 composition of FA. The presence of amorphous phases in Fig. 7 can be recognized by the

17 broad hump beneath the diffraction peaks of the crystalline phases centred around 34 2theta

18 (detailed offset made patterns visible in the same graph, Fig 7). The amorphous phase content

19 decreased for carbonated S50 sample, compared to the reference S50 sample (Fig. 8).

1   Carbonation of the reaction products in S50 paste has resulted in the formation of vaterite and

2   calcite. The same carbonation products were identified for S30 and S70 exposed samples.

3   The quantitative phase analysis is given in Fig. 8, where the results are normalised to

4   100 %. The major phase in pastes was amorphous (> 70 wt.%) for both, reference and

5   samples exposed in the natural laboratory conditions. The reference samples consisted of FA

6   or FA and GBFS, have similar phases, whereas the amorphous content increased with an

7   increase of GBFS. In the sample S100, no other phases except minor traces of calcite (< 0.5

8   wt.%) were identified for both reference and exposed samples, indicating that reaction

9   products were not carbonated. Similarly, reaction products in sample S0 did not undergo

10   carbonation, such as shown in Section 3.3. However, sodium-based carbonates, natron

11   ($Na_2CO_3*10H_2O$) and nahcolite ($NaHCO_3$), were identified in the exposed S0 sample, as a

12   products from the carbonation of pore solution. In addition, amorphous phase proportions

13   were found to be different for reference and exposed S0 samples. Higher content of the

14   amorphous phase in the reference S0 sample, was attributed to the curing conditions. The

15   reference samples were kept in the sealed conditions until the testing. No water exchange was

16   possible between the sample and environment, which most likely contributed to higher

17   reaction degree and higher amount of the reaction products in reference S0 sample, compared

18   to the carbonated sample. On the other hand, content of the carbonation products in S30, S50

19   and S70 pastes, were 10.1, 14.5 and 11.2 wt. %, respectively. Rietveld quantification of

20   phases revealed that the proportion of vaterite was dominant (Fig. 8). Vaterite is well known

21   as an unstable precipitate in supersaturated solutions, caused by a nonstoichiometric reaction

22   conditions as showed by Jung et al. [40]. The nucleation of different calcium carbonates is

23   reported to be dependent on the supersaturation level, ionic ratio of $[Ca^{2+}]/[CO_2^{3-}]$ in solution

24   and the pH of solution [40-42]. According to Hostomsky et al. [43], precipitation of vaterite in

25   the reaction of calcium nitrate and sodium carbonate occurs at pH$\geq$ 9.5, but calcite is obtained

1   at pH≤ 8.5. In addition, Kralj et al. [42] reported precipitation of pure vaterite from the

2   solution of calcium chloride and sodium carbonate at 9.3 ≤pH≤ 9.9. Regarding carbonation as

3   a continuous process followed by a pH decrease, the unstable vaterite might re-crystallize into

4   stable calcite if there is a sufficient moisture [44]. The re-crystallization of vaterite in this

5   study was not the case and it was most probably inhibited by the moisture content (55% RH),

6   but also due to the pH level of the pore solution. The pH of pore solution in AAM after

7   carbonation is generally maintained above 9 due to high carbonate/bicarbonate ratios as

8   showed by Bernal et al. [45] in the natural carbonation conditions, which were the conditions

9   studied in this paper.

10   In contrast to vaterite and to less extent calcite identified in this study, calcite is the

11   main carbonate beside aragonite and vaterite, formed from the natural carbonation of OPC-

12   based paste as found by Hidalgo et al. [46]. Accordingly, the formation of more vaterite than

13   calcite in this study can be partially attributed to the nanostructural ordering and

14   thermodynamic stability of the C-(N)-A-S-H gel in alkali-activated pastes, compared to C-S-

15   H gel in OPC-based pastes. White et al. [47] have investigated intrinsic differences in atomic

16   ordering of calcium (alumino) silicate hydrates in conventional and alkali-activated cements.

17   The authors found large intrinsic differences in the extent of nanoscale ordering between C–

18   S–H derived from C_3S and alkali-activated GBFS systems using X-ray total scattering. It is

19   showed that C-(N-)A-S-H gel is mostly amorphous and intrinsically less thermodynamically

20   stable than (nano)crystalline C_3S-based gels. This implies different phase dissolution

21   mechanism regarding carbonation of AAM compared to OPC-based materials, which results

22   in precipitation of different $CaCO_3$ polymorphs. In this regard, by comparing the main

23   carbonation products in AAM as from this paper (vaterite) with carbonation products from

24   OPC-based materials [46] (calcite), both from the natural laboratory conditions, it is showed

25   that the previous implication is valid.
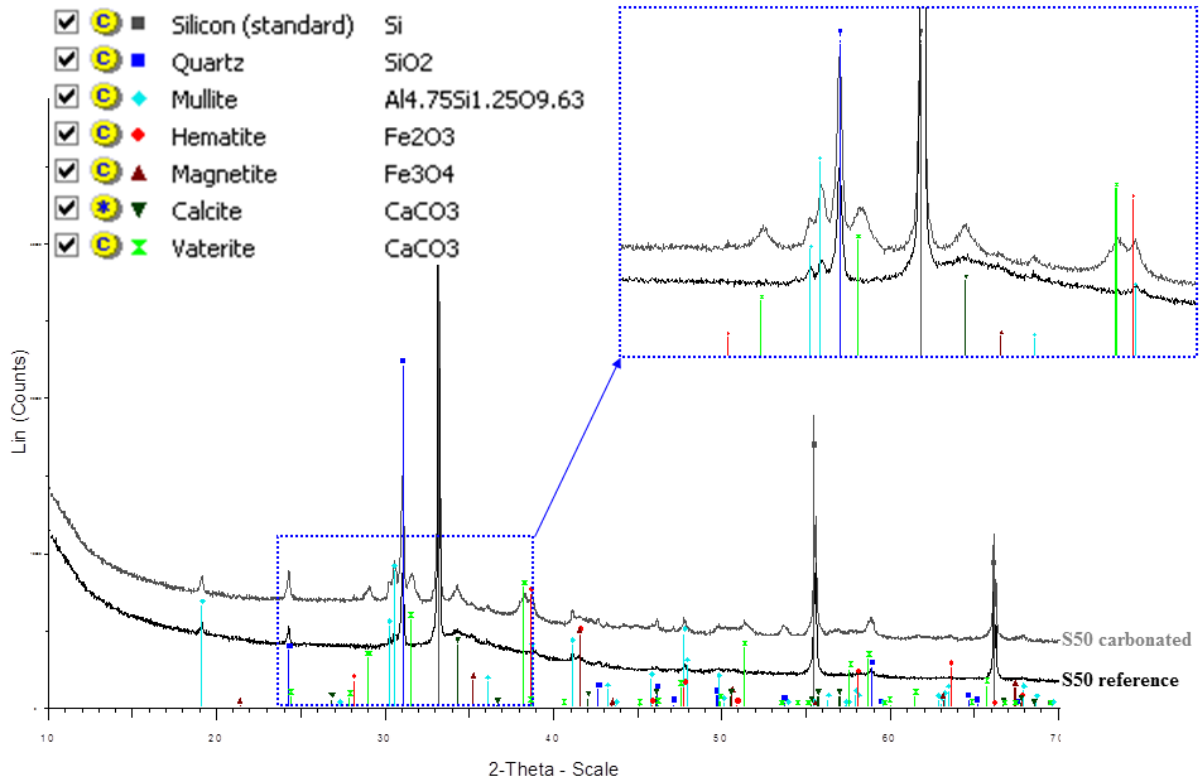
Fig. 7. Comparison of the XRD scans with respect to the phases in reference and carbonated S50 paste.
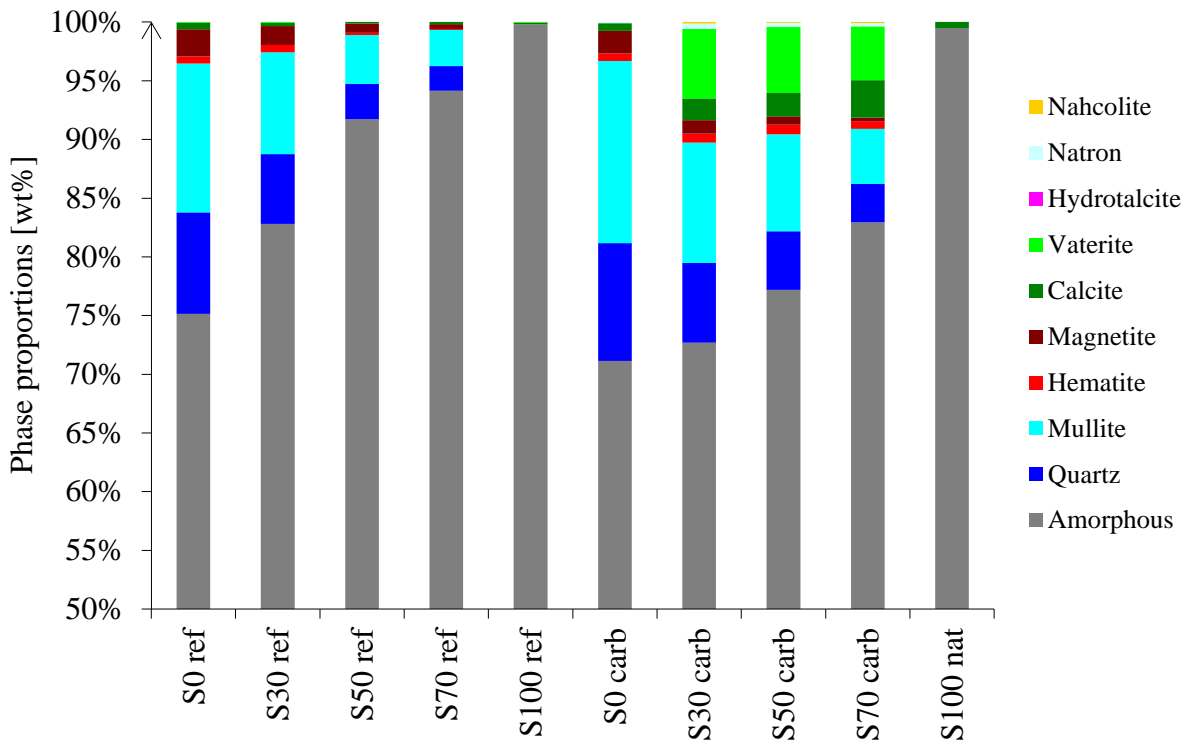
1   **Fig. 8.** Quantitative phase analysis by Rietveld method for reference pastes and for the pastes

2   exposed in the natural laboratory conditions.

3   3.2.   Decalcification degree determined by SEM-EDX

4   Fig. 9 demonstrates the contrast of microstructures between reference pastes and

5   pastes exposed in the natural laboratory conditions. In reference pastes, more uniform and

6   denser microstructure is formed with a higher GBFS content. In the carbonated areas in the

7   samples S30, S50, S70 four main features can be observed (Fig. 9, *b-ii, c-ii, d-ii*): (1) pores

8   and microcracks, (2) carbonated gel with decrease in average atomic mass, (3) noncarbonated

9   gel isolated from the carbonated part, (4) unreacted FA and GBFS particles. This is in

10   agreement with a previous study of Sisomphon et al. [48], who observed a similar morhology

11   of the carbonated microstructure in GBFS mortars (made by CEM III/B 42,5 N and CEM I

12   42,5 N) after 1 year of carbonation in the natural atmospheric conditions. The difference of

13   gel greyscale levels in backscattered electron (BSE) images between noncarbonated and

14   carbonated areas (Fig. 9, b-ii, c-ii, d-ii), is attributed to their different nanoporosities and

15   therefore to different densities and backscattered electron coefficients, as found by Famy et al.

16   [49]. The samples S0 and S100 were not carbonated, which can be clearly seen when the CO_2

17   exposed microstructures are compared to the corresponding reference microstructures.

18   Therefore, only blended pastes (S30, S50, S70) have been further studied by SEM-EDX for

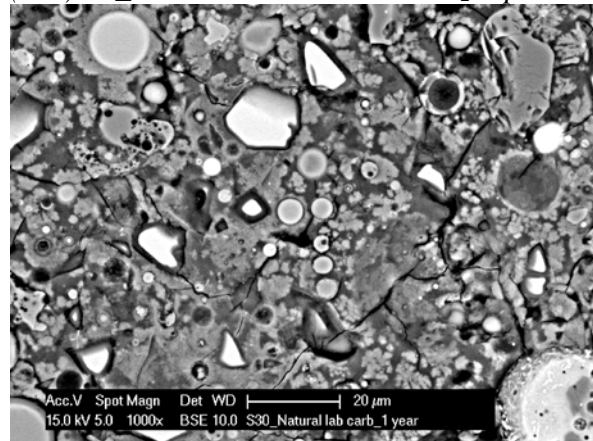19   the chemical analysis, since only in these samples the gel was carbonated.
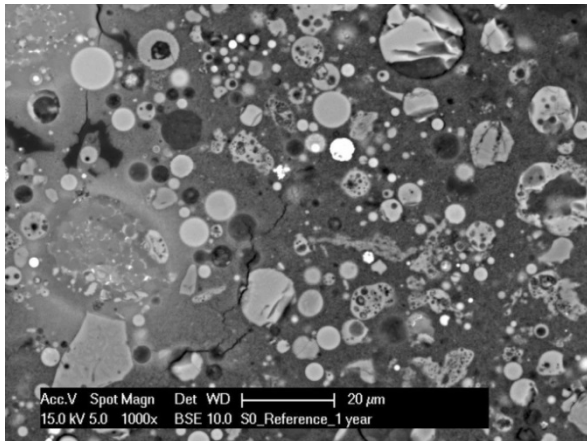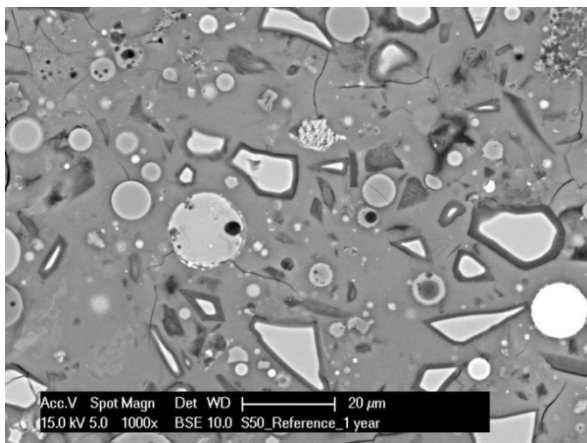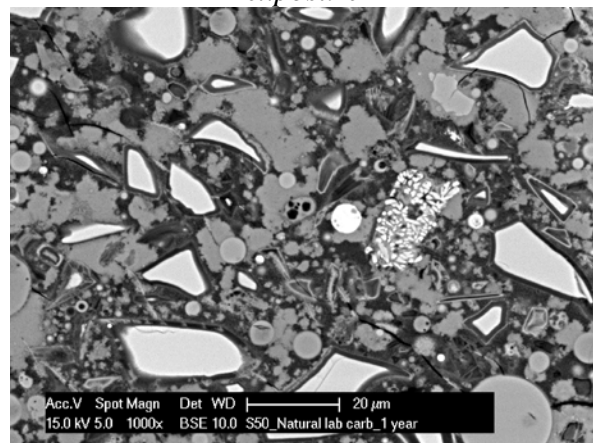
(a-i) S0_ reference
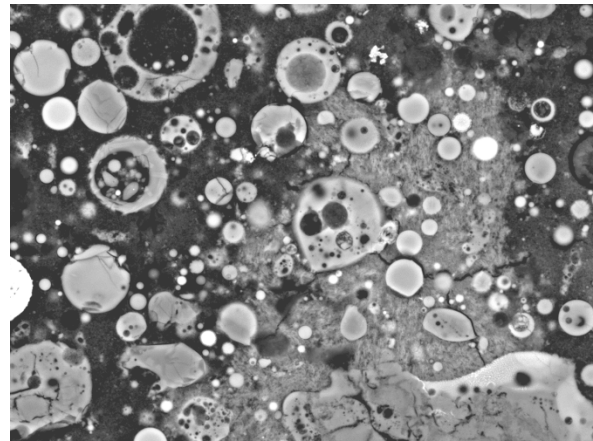
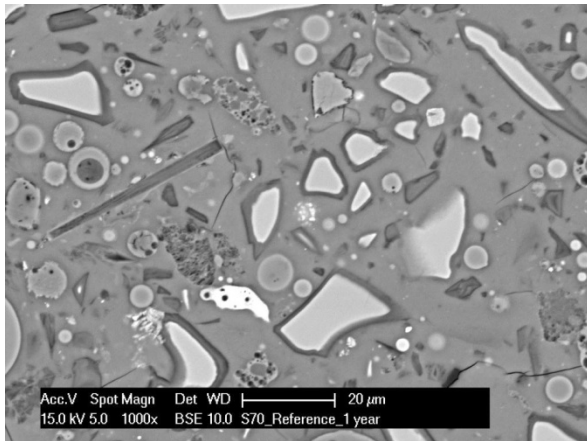*(a-ii) S0_noncarbonated under CO$_2$ exposure*
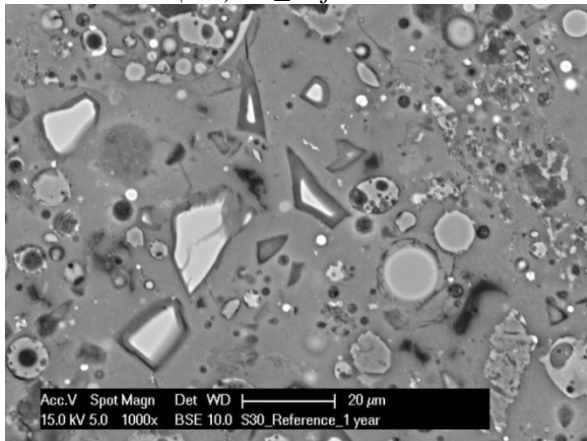
(b-i) S30_ reference

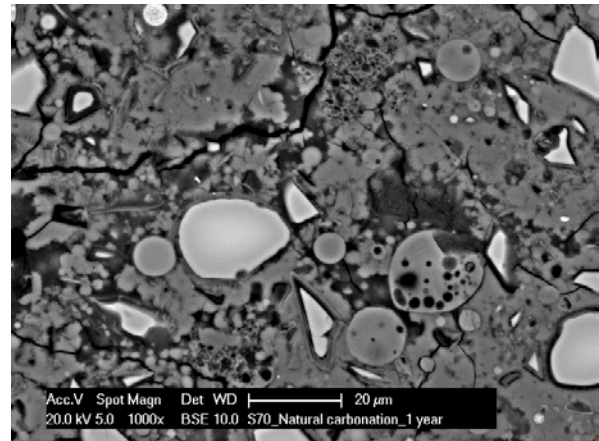*(b-ii) S30_ carbonated area under CO$_2$ exposure*
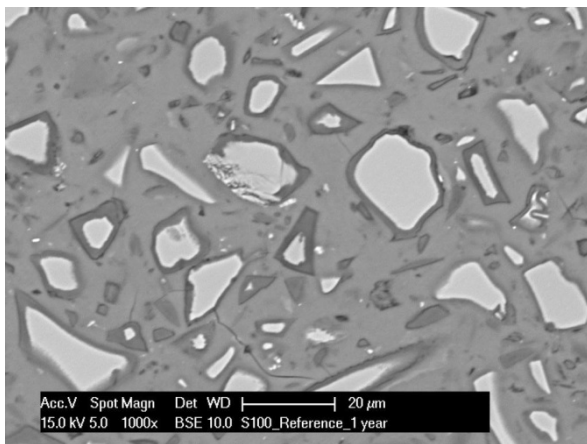
(c-i) S50_ reference

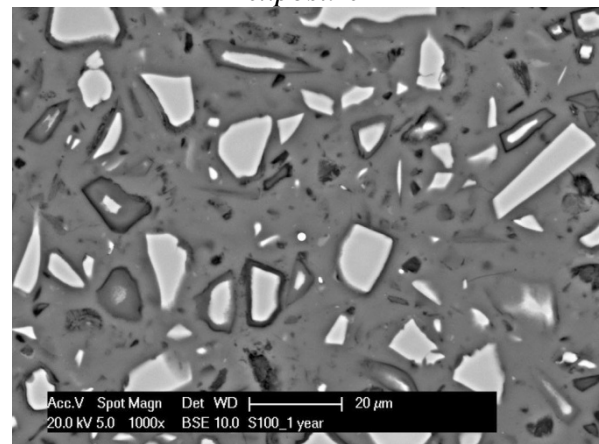*(c-ii) S50_ carbonated area under CO$_2$ exposure*

(d-i) S70_ reference

(d-ii) S70_ carbonated area under CO_2 exposure

(e-i) S100_ reference

(e-ii) S100_noncarbonated under CO_2 exposure

1

2 **Fig. 9.** SEM-BSE images of *(i)* the microstructures of reference samples, *(ii)* the

3 microstructures of samples after 1 year of exposure in the natural laboratory conditions.

4

5 The EDX spot analyses were made for carbonated and noncarbonated areas (Fig. 9, *b-*

6 *ii, c-ii, d-ii*). In order to study the elemental composition, parameters for consideration

7 regarding the chemical changes are firstly discussed. The primary carbonation reaction is a

8 sample surface reaction between dissolved CO_2 gas and pore water. When the dissolved CO_2

9 molecules diffuse into the material, the pH of the pore solution decreases due to the formation

10 of carbonic acid. When the pH decreases to 12, the equilibrium between pore solution and the

11 reaction products is disturbed and the weakest bounded elements will be decomposed from

12 the gel structure. The Ca^{2+} ions are the first to be decomposed and migrated into the pore

1   solution. The saturation of the pore solution with Ca^{2+} ions and with salts of the carbonic acid

2   will eventually result in calcium carbonates precipitation [50]. The carbonation reaction

3   degree will be limited by the gel solubility, calcium content, the bulk pore volume and ion

4   concentration in the pore solution. If the carbonated pore solution is saturated with Ca^{2+} ions,

5   the gel will be preserved from further decomposition. This can be due to reduced pore volume

6   or high Ca content in the precursor. For instance, paste S100 has the lowest porosity (~3.68%)

7   amongst the tested pastes, as shown in Table 3, suggesting the lowest amount of the pore

8   solution. In addition, this paste has the highest Ca content (Table 3), but its microstructure is

9   not carbonated at all. Therefore, in such a dense system, the pore structure will be governing

10   factor and, irrespectively of the binder chemistry, will limit the carbonation degree. On the

11   contrary, paste S0 has the lowest Ca content and the largest porosity which enables CO_2

12   molecules to diffuse faster and dissolve in the pore solution of this sample. Moreover, it is

13   reported that the gel in alkali-activated FA cannot be carbonated [51], and that carbonation of

14   alkali-activated FA is mainly limited to the pore solution. Therefore, both chemistry and pore

15   structure of the individual systems need to be considered when carbonation degree is to be

16   determined.

17   **Table 3**

18   Summary of the important pastes properties for understanding the carbonation mechanism.

Mixture	pH of the pore solution at 28 days [52]	Ca-content from FA and GBFS (by mass weight), determined by XRF	Critical pore diameter at 28 days (nm), determined by MIP or N2 [52]	Porosity at 28 days (percentage of the bulk volume, MIP) [52]
S0	13.45	4.8	110 (MIP)	37.06
S30	13.48	15.30	30 (N_2 adsorption)	14.87
S50	13.76	22.30	4 (N_2 adsorption)	7.48
S70	13.83	29.3	4 (N_2 adsorption)	6.65
S100	13.97	39.8	6 (N_2 adsorption)	3.68

1   The atomic ratios for the primary elements in the noncarbonated and carbonated areas are

2   given in Table 4. The areas were tested in such a way that the unreacted FA and GBFS

3   particles, or the rims between single particle and the surrounding matrix were excluded from

4   the EDX spot analyses. However, due to possible cross-contamination of the EDX spectra, the

5   lowest atomic ratios indicated by the extremity of the data cluster are reported in Table 4.

6   Regardless of the GBFS content in this study, the Na/Si ratio in the carbonated gel did not

7   change significantly compared to the noncarbonated gel (Fig. 10). The Na/Si ratio for S50 and

8   S70 is higher than for the S30 sample. In pastes with 50 wt.% or more GBFS, it is assumed

9   that the reaction is more intense and more reaction products are formed, consequently

10   absorbing more Na ions in their molecular structures. The Mg/Si ratio showed significant

11   variations in the distribution for S50 and S70 samples compared to the sample S30. The S30

12   sample has the same Mg/Si ratio for both measured areas, i.e. carbonated and noncarbonated,

13   because its composition consisted of only 30 wt.% of GBFS and the results suggest that Mg

14   has not formed other reaction products except being distributed in the gel. The results of

15   Mg/Si ratio for S50 and S70 pastes suggest that the Mg is sporadically distributed throughout

16   the gel and that some other reaction products consisting Mg, such as hydrotalcite showed by

17   Haha et al. [53], are intermixed with the gel, causing the data scattering.

18   Marked decalcification (the last column in Table 4) had occurred in all blended pastes.

19   The Ca/Si ratio has been reduced for the carbonated areas compared to the noncarbonated

20   areas, but the gel was not completely decalcified. Instead, carbonation lowered the Ca/Si ratio

21   until a certain value, which is the lowest for sample S50. Although it was expected that S70

22   sample has a higher decalcification degree since it has a higher Ca amount than S50, the

23   findings show that the decalcification degree was lower. This is most likely due to the finer

24   pore structure of S70 sample compared to S50 sample, which hinders the CO_2 diffusion.

25   **Table 4**

1   Atomic ratios determined for the two areas of the samples by EDX analyses.

Sample	EDX area	Na/Si	Mg/Si	Ca/Si
S30	noncarbonated	0.1	0.05	0.7
	carbonated	0.1	0.05	0.2
S50	noncarbonated	0.25	0.03	0.9
	carbonated	0.25	0.03	0.1
S70	noncarbonated	-	0.07	0.8
	carbonated	-	0.07	0.2

2
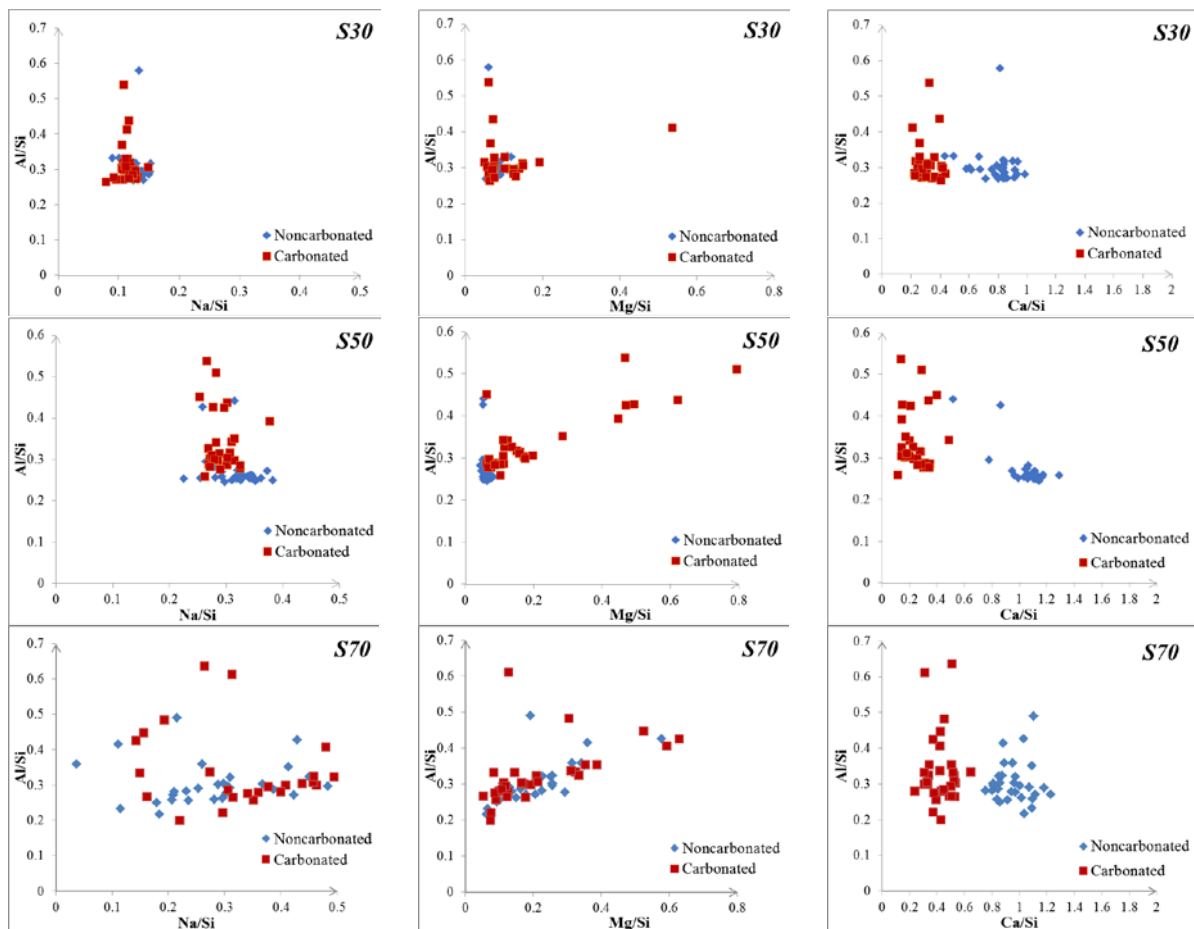
3
4   **Fig. 10.** The 2D scatter plots of EDX point analyses with different element atomic ratios in

5   the carbonated and noncarbonated areas of the samples that were exposed in the natural

6   laboratory conditions.

7   3.3.   Polymerization degree determined by ATR-FTIR

8   The polymerization of the remaining hydrous silica gel after gel decalcification is

9   demonstrated in the Fig. 11. ATR-FTIR can provide valuable information on the chemical

bonds of the silicates in the amorphous material, which is difficult to be studied by XRD. The Si-O stretching modes for the SiQ^n units show infrared absorption bands localized around 1100, 1000, 950, 900, and 850 cm^{-1} for n = 4, 3, 2, 1, and 0, respectively [54]. These values shift to higher wavenumbers when degree of silicon polymerization increases, such as found in the carbonated phases of cementitious materials [18]. In this study, ATR-FTIR measurements are used to identify new bands corresponding to carbonation products and to observe the change of the primary silicate bands. The analysis was based on comparison between reference and carbonated samples of alkali-activated pastes.

The infrared spectra of the unreacted FA and GBFS pastes are shown in Fig. 11, in the spectra of samples S0 and S100 (red lines). The main band for unreacted FA is found at 1046 cm^{-1}, which is assigned to Si-O-T bands, while weaker bands were identified at 798, 780, and 695 cm^{-1} indicating the presence of quartz [55]. On the other hand, the unreacted GBFS shows the main vibration band located at 905 cm^{-1}, which is due to the asymmetric stretching vibration of terminal Si-O bands. The evolution of the spectrum when FA was activated is mainly seen as a shift of the stretching band (1046 cm^{-1} for unreacted FA), to lower wavenumber (980 cm^{-1} for alkali-activated FA), while for alkali-activated GBFS a shift of the stretching band (905 cm^{-1} for unreacted GBFS) was to higher wavenumber (945 cm^{-1} for alkali-activated GBFS). This shift was monitored for different curing ages (28, 180, 393 days), and is attributed to the formation of the amorphous gel phase after alkaline activation. Samples S0 and S100 were also analysed after 1 year in the natural laboratory conditions and compared to the corresponding reference samples that were sealed for 1 year (without CO_2). Comparing the FTIR spectra's features, there was no significant difference between reference and exposed S0 sample, manifesting that the N-A-S-H gel does not react with ionic carbonic acid in the natural laboratory conditions, as found by Bernal et al. [51]. Only a weak peak at 1444 cm^{-1} was found as a new peak that can be assigned to v^3 CO (CO_3^{2-}) band. Similar to

1 sample S0, sample S100 after 1 year in the natural laboratory conditions did not undergo

2 chemical changes, which can be seen from the comparison to the sample that was sealed for 1

3 year, suggesting no carbonation effect on the main structure of the gel. This is attributed to the

4 low porosity of the sample S100 that did not allow CO_2 molecules to diffuse into the material,

5 supported by N_2 adsorption measurements in the section 3.4.

6   Regarding blended pastes (S30, S50, S70), their reference spectra for samples at 28,

7 180, 393 days have the main band assigned to Si-O stretching vibrations of the SiQ^2

8 tetrahedra located at 960, 953, 947 cm^{-1}, which shifts to lower wavenumbers with increasing

9 GBFS content, i.e. with increasing Ca/Si ratio, indicating progressive depolymerisation of the

10 silicate chains as reported by Yu et al. [56]. In Fig. 11, the spectra of the samples exposed for

11 1 year in the natural laboratory conditions have the main band that was shifted progressively

12 towards higher wavenumbers from 947 cm^{-1} to 996 cm^{-1}. The shift to higher wavenumbers

13 indicates the presence of more polymerised units, as the calcium is removed indicating silicate

14 polymerization upon C-(N-)A-S-H gel decalcification. The excess of negative charge in the

15 gel due to Ca^{2+} removal, was balanced through adsorption of alkalis (OH^-, Na^+) in the

16 decalcified C-(N-)A-S-H gel and formation of Si-OH or Si-O-Na groups. Condensation of

17 neighbouring groups Si-OH or Si-O-Na into Si-O-Si moves the system towards the

18 equilibrium, forming silicate gel. The very broad absorption bands (900–1200 cm^{-1}) of

19 carbonated samples S30, S50 and S70, indicated the amorphous character of the silicate gel as

20 showed in [57]. Spectra of the carbonated samples S30, S50 and S70 contain also new

21 features, which can be associated with the formation of carbonates with different intensities

22 indicated by the presence of the large bands near 713, 740, 858, 874, 1420 and 1490 cm^{-1}

23 (Fig. 11, Table 5). The intensity of the carbonate peaks are higher in S50 sample comparing to

24 that of S30 and S70 samples. Therefore, S50 sample is the most vulnerable to carbonation.

25 The results are in agreement with SEM-EDX findings.

| Band assignments	FA	GBFS	S0		S30		S50		S70		S100	
	raw	raw	R	NLC	R	NLC	R	NLC	R	NLC	R	NLC
v^4 CO (CO_3^{2-}) (calcite)	-	-	-	-	-	713	-	713	-	713	-	-
v^4 CO (CO_3^{2-}) (vaterite)	-	-	-	-	-	-	-	740	-	740	-	-
v^2 CO (CO_3^{2-}) (vaterite)	-	-	-	-	-	858	-	858	-	858	-	-
v^2 CO (CO_3^{2-}) (vaterite)	-	-	-	-	-	874	-	874	-	874	-	-
v Si–O Q^2	-	890	980	994	960	-	953	-	947	-	945	-
v^3 Si–O	1050	-	-	-	-	990	-	996	-	995	-	-
v^3 CO (CO_3^{2-}) (vaterite/calcite)	-	-	-	1440	-	1420 1480	-	1420 1480	-	1420 1480	-	-
δ OH (H_2O)	-	-	1642	1642	1644	1644	1642	1642	1642	1642	1646	1646

5

6

1

2

3

4
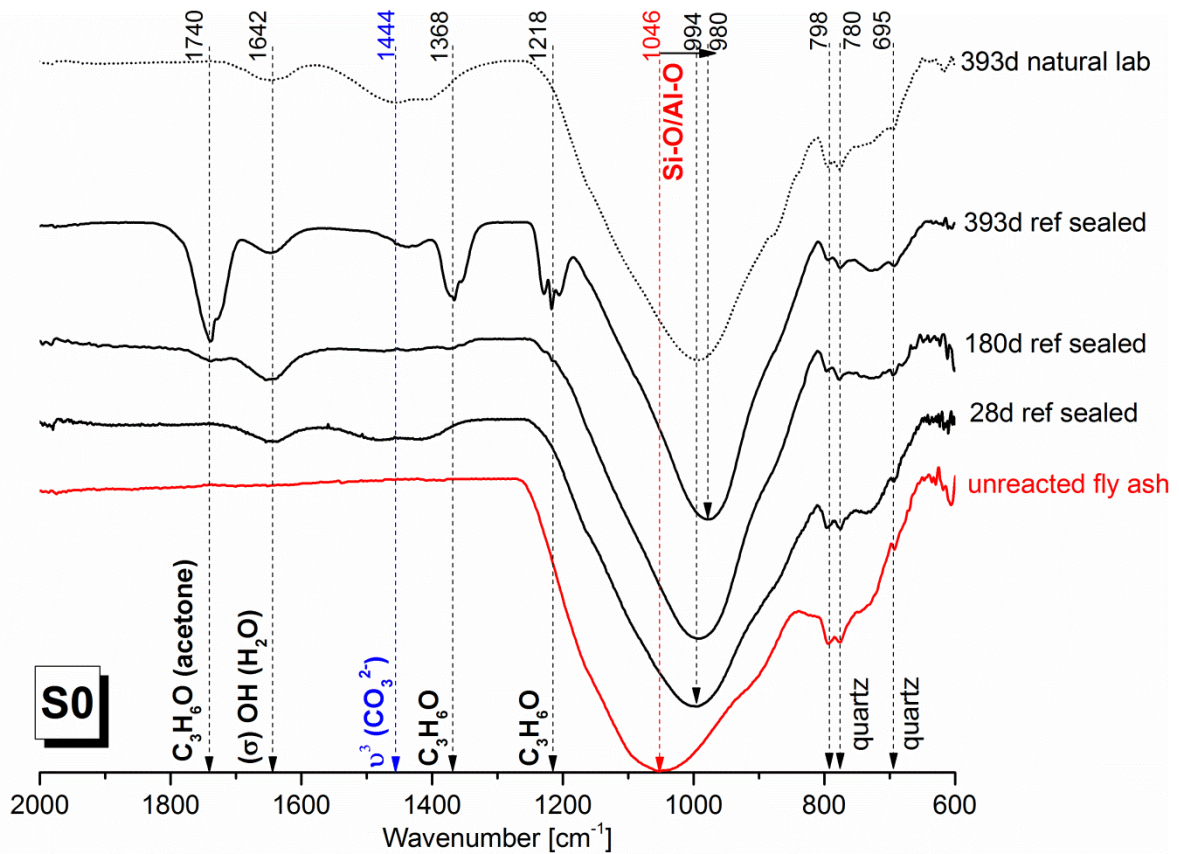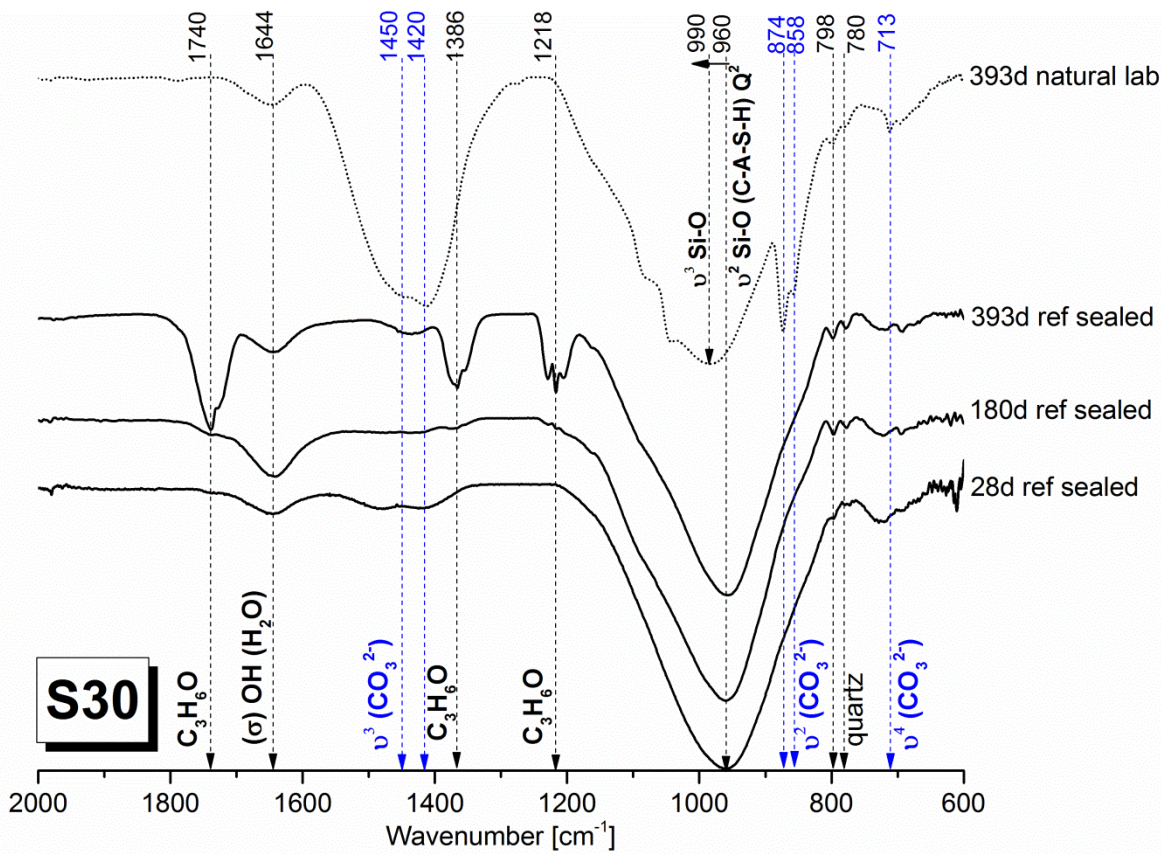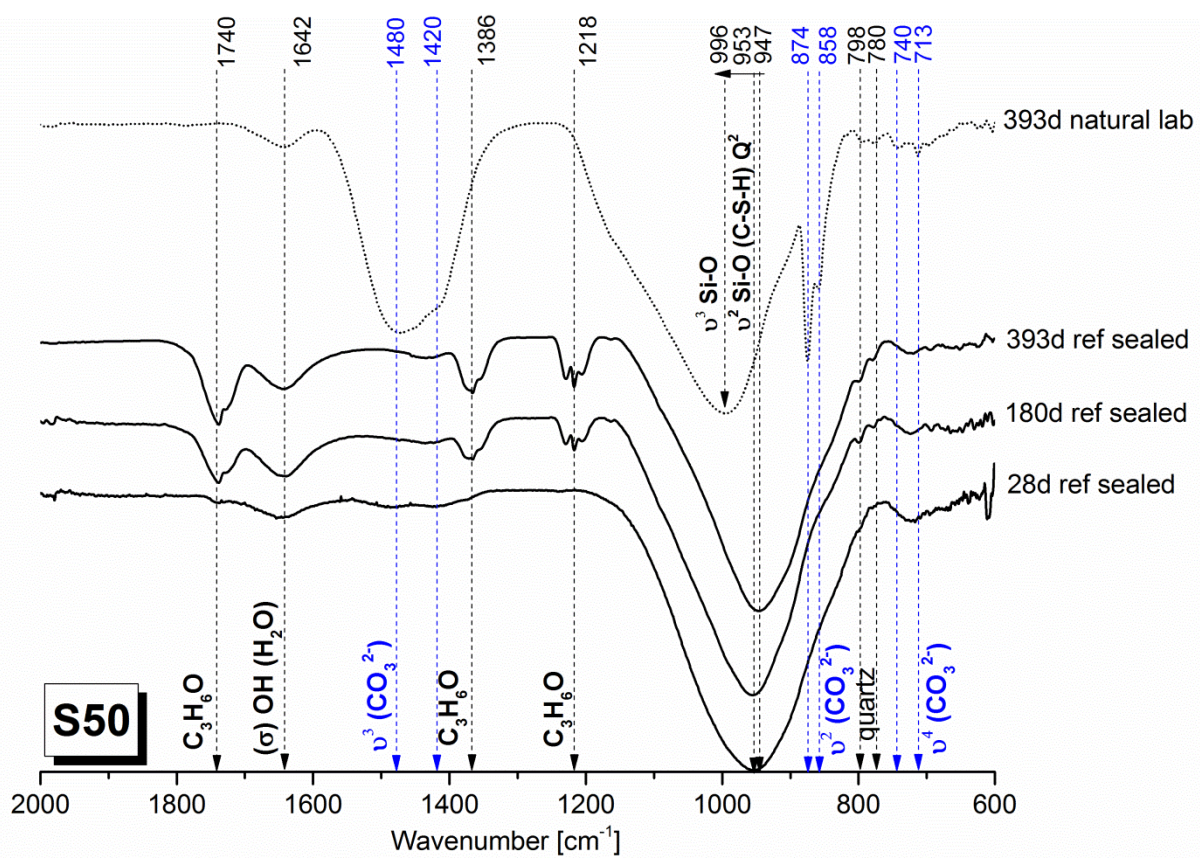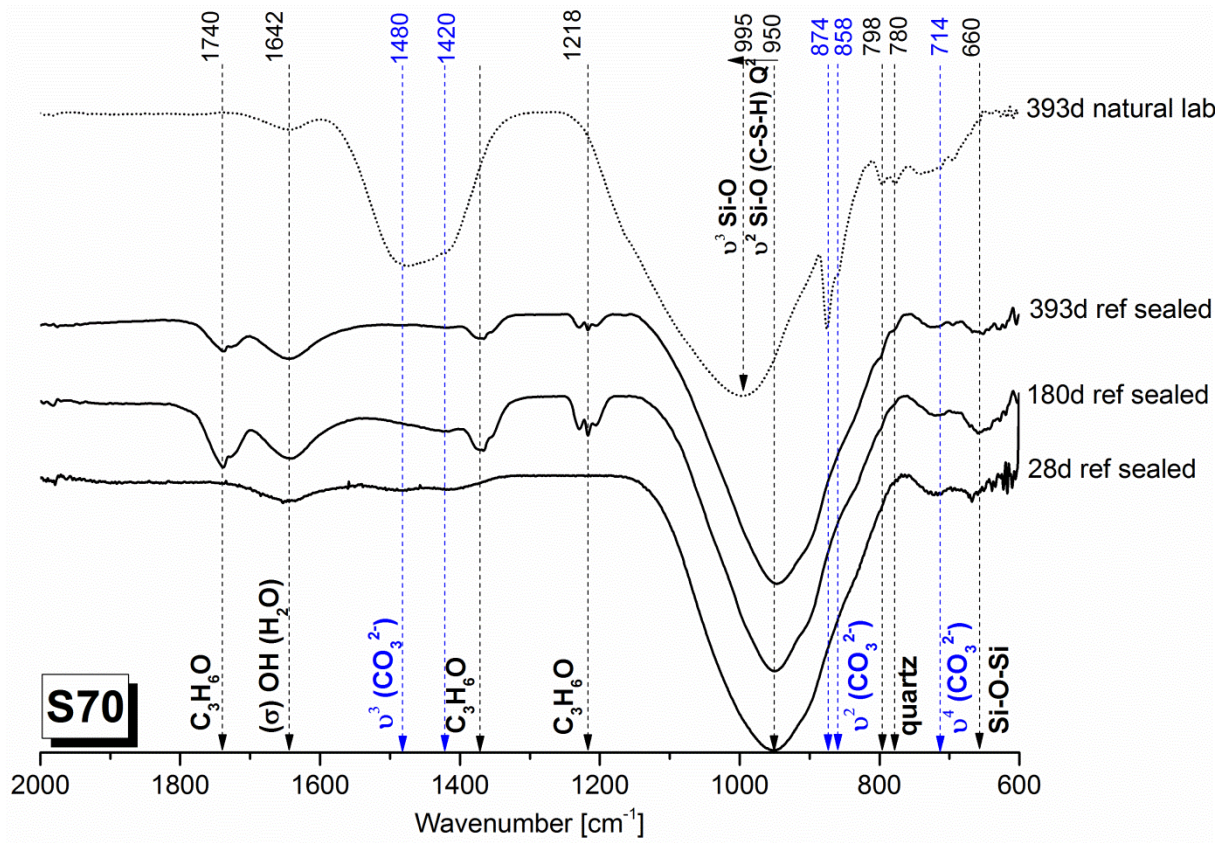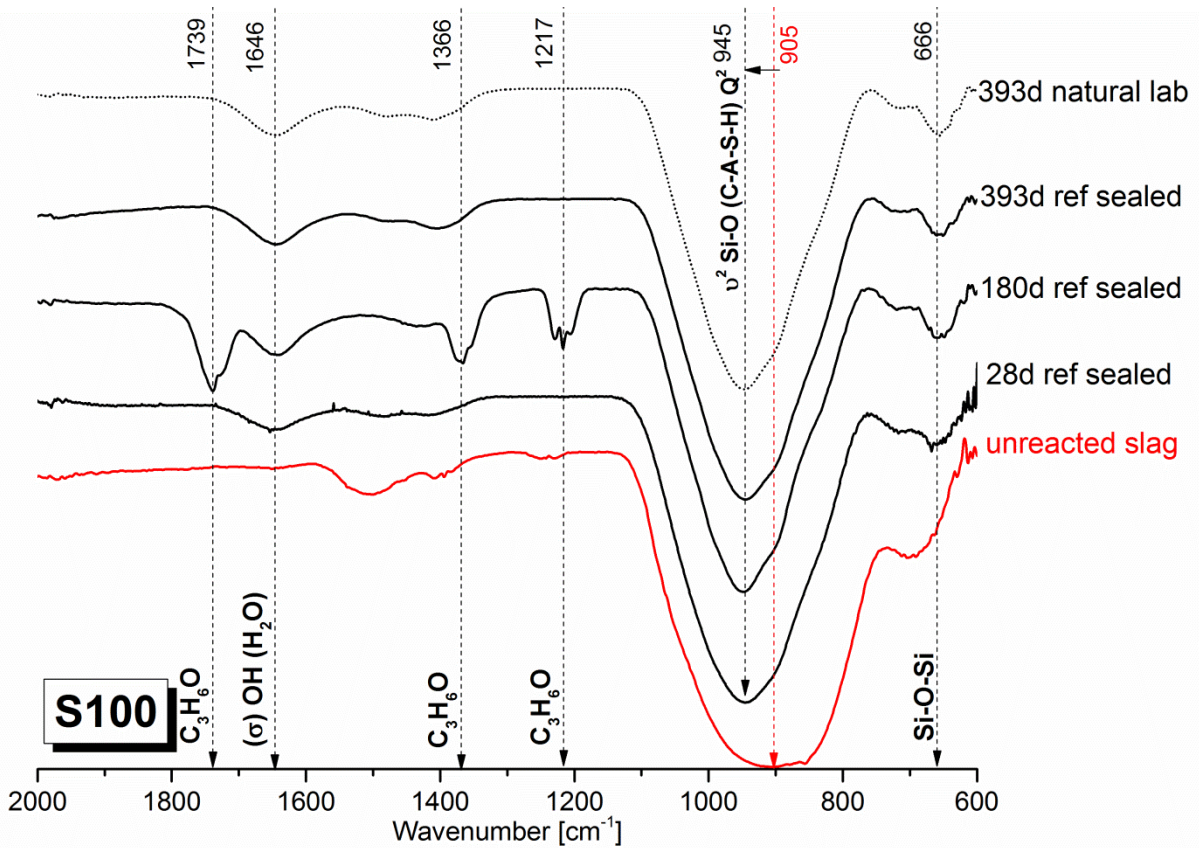
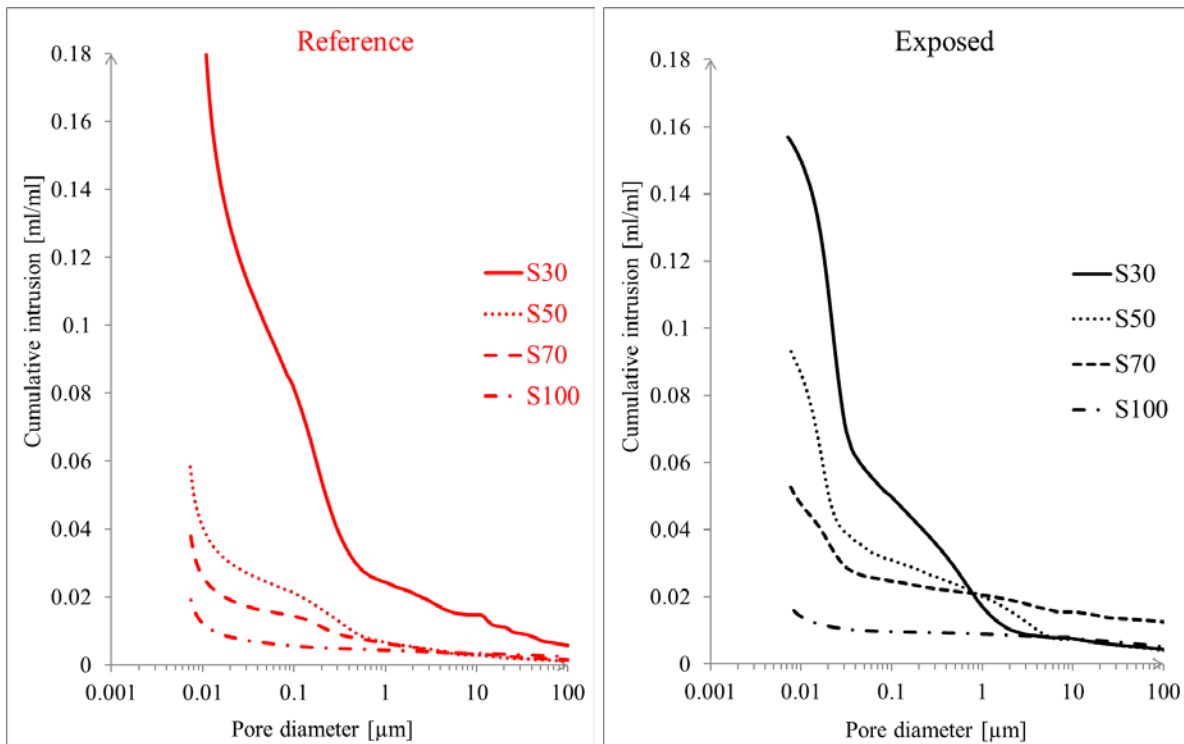**Fig. 11.** Infrared spectra of alkali-activated pastes.

3.4. Pore structure by MIP and N_2 adsorption

Pore size and pore size distribution measurements were performed for the reference pastes and for the pastes exposed in the natural laboratory conditions. The MIP results for all mixtures and the main pore structure characteristics are summarized in Table 6, while cumulative intruded pore volume curves and corresponding pore size distributions obtained for carbonated and reference samples are presented in the Fig. 12. Total porosity and threshold pore diameter of the pastes with higher GBFS content decreases. The physical meaning of a threshold pore diameter reported in Table 6 is that the pores with the diameter greater than this cannot form a connected path through the sample [58]. It should be noted that the threshold pore diameter could not be determined for reference samples and for some of the samples exposed to CO_2 (S70, S100), suggesting very dense microstructures. The MIP tests for sample S100 after 1 year of the exposure, have shown no significant change in the volume of capillary pores, compared to the reference samples (no carbonation). However, sample S0 exhibited a decrease in total porosity, probably due to formation of sodium carbonates as found by XRD (Fig. 8) and their precipitation in the pore space. Although, sodium-based carbonates were identified, their content is not enough to justify such a decrease of the total porosity in carbonated S0 sample, compared to the reference S0 sample. It is believed that sodium-based carbonates were leached out during sample preparation due to their high solubility and high porosity of S0 paste (~40% v/v), before the pore structure properties of the samples have been tested. On the other hand, S50 and S70 samples have an increased total porosity (Fig. 12). This increase is attributed to the formation of porous silicate gel after the C-(N-)A-S-H gel has been decalcified. In order to study the effect of carbonation on the gel pore size distribution (PSD) N_2 adsorption method was used.
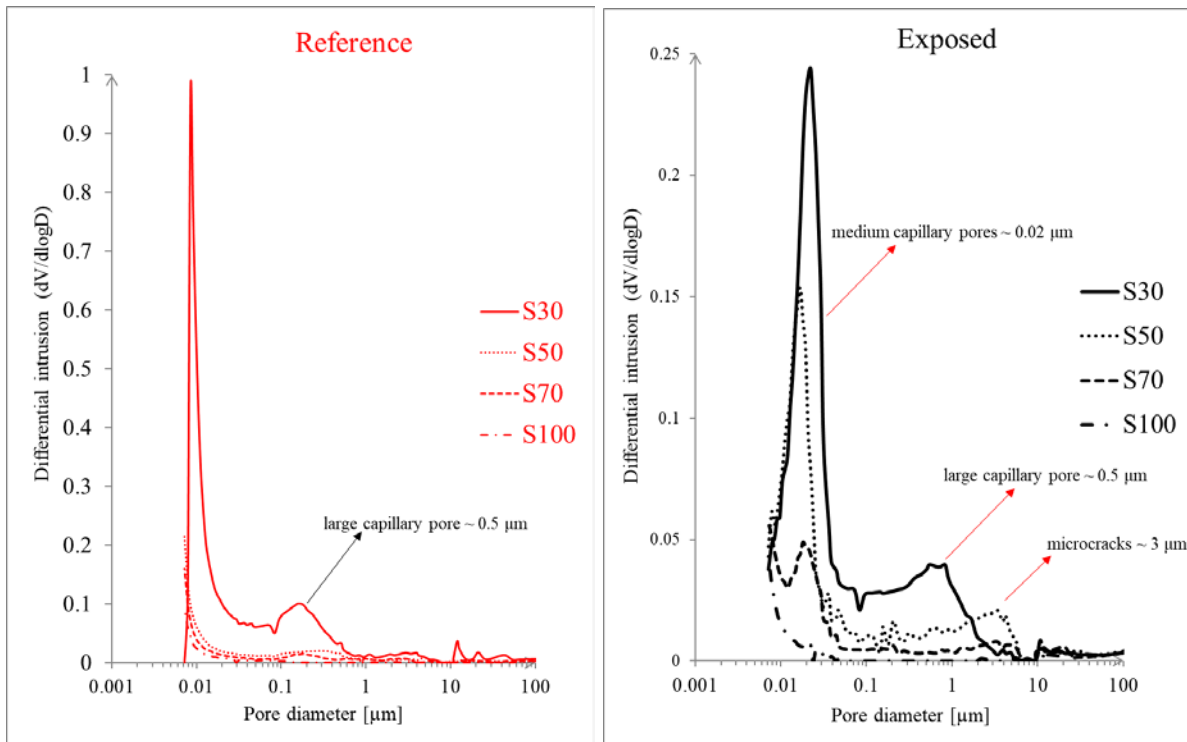
1 **Table 6**
2 Capillary pore structure properties by MIP.
3

Mixtures	Threshold pore access diameter (µm) Reference	Threshold pore access diameter (µm) Carbonated	Total porosity [%] by volume Reference	Total porosity [%] by volume Carbonated
S0	0.120	0.134	30.41	43.72
S30	-	0.03	26.04	26.22
S50	-	0.028	9.404	17.09
S70	-	0.026	6.538	9.66
S100	-	-	3.57	3.38

4

5

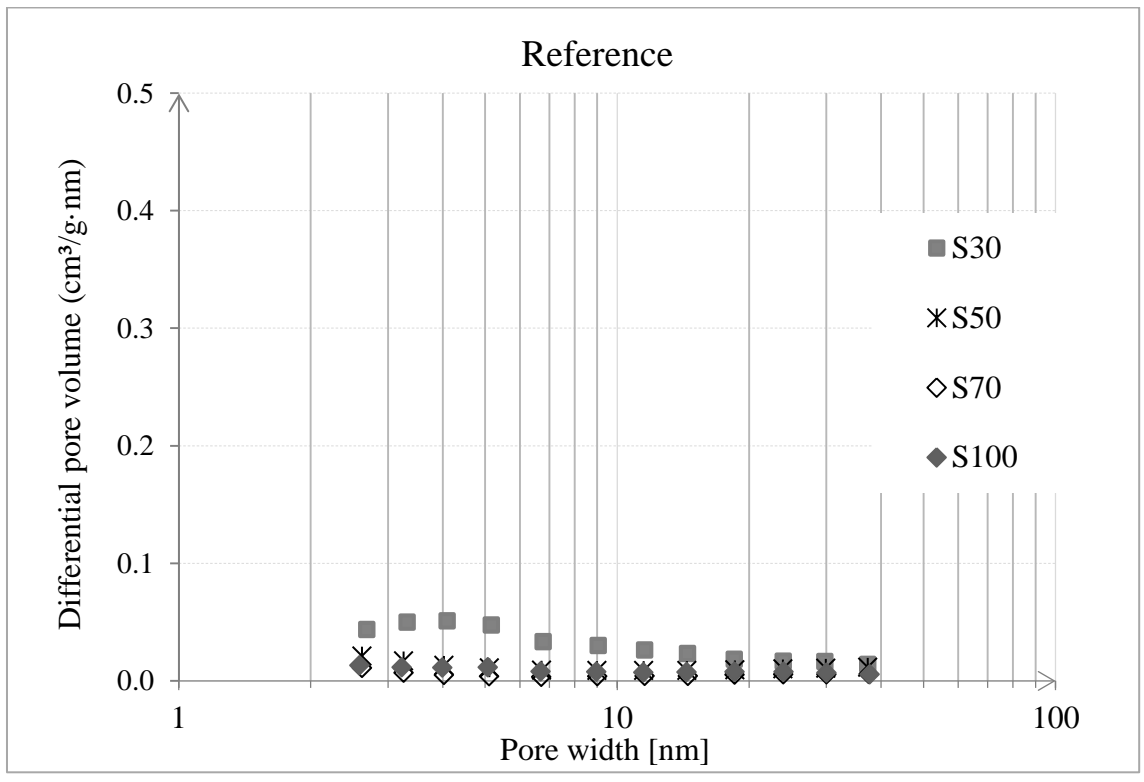**Fig. 12.** MIP Capillary pore volume and pore size distribution (reference and exposed samples after 1 year).

N_2 adsorption measurments are shown in the Fig. 13. The results are summarized in Table 7. The PSD indicates a dense microstructure for sample S100, where CO_2 can hardly diffuse and react with phases. The gel porosity of the pastes decreases with increasing GBFS content. As the SEM images showed (Fig. 9), there will be more restriction on diffusion in GBFS-rich than through FA-rich pastes. The largest differences in the pore size and volume between reference and exposed samples were found for pastes S30 and S50. The main change is in BET surface area, i.e. increase of the gel pores surfaces (Table 7). For instance, the results have shown that carbonated S50 sample has a significantly higher BET surface area compared to the reference sample. This increase is attributed to the widening of the gel pores due to the gel decalcification and polymerization of silicate chains.

Table 7
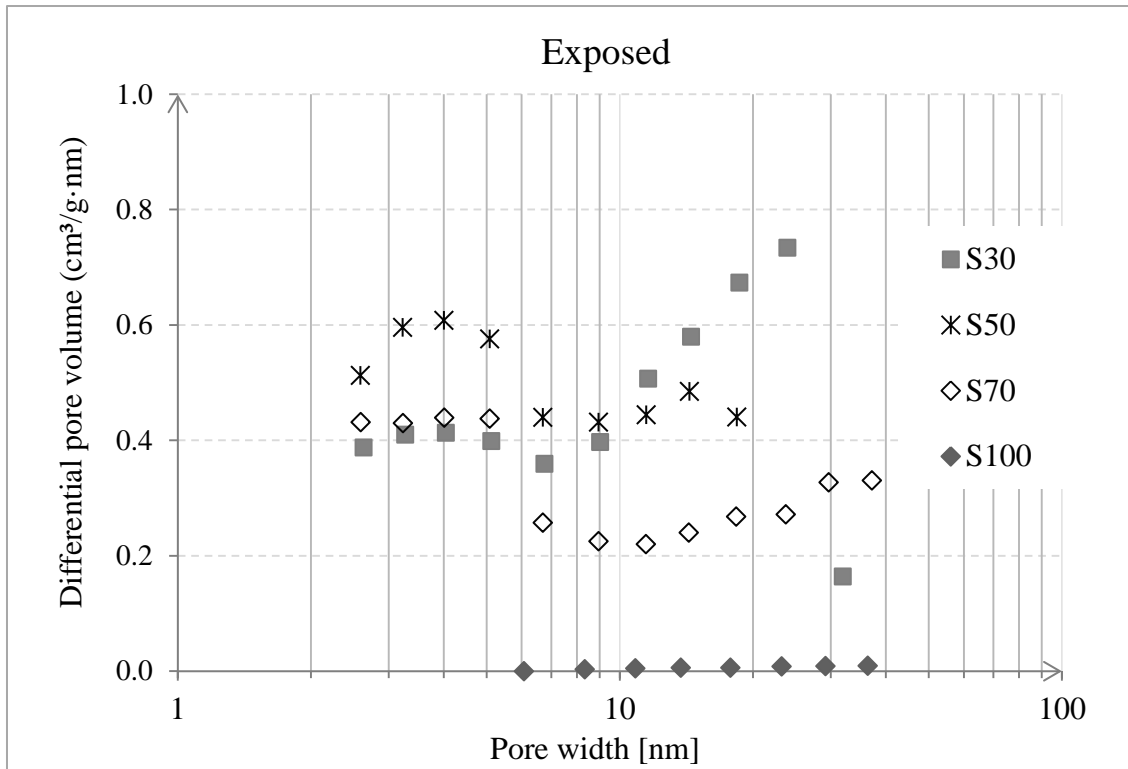Gel pore structure properties by N_2 adsorption, evolution of the BET surface area.

Mixtures	Threshold pore access diameter (nm) Reference	Threshold pore access diameter (nm) Carbonated	BET surface area [m²/g] Reference	BET surface area [m²/g] Carbonated
S0	12	-	15.85	6.71
S30	5.52	7.29	2.58	27.91
S50	6.16	7.47	1.57	34.89
S70	6.57	6.25	0.88	25.1
S100	6.01	-	0.78	0.25

1

2

1

Fig. 13. BJH pore size distributions in reference samples (upper photo) and exposed samples

(photo below) after 1 year.

3.5.   Nanoindentation modulus (E_m)

The area of indents is visualized by the optical microscope for the samples S50 (Fig.

14a) and S100 (Fig. 14b). Both mixtures have the grey/brownish background which is the gel

phase. The brightest uneven shaped particles are the unreacted GBFS particles, and the

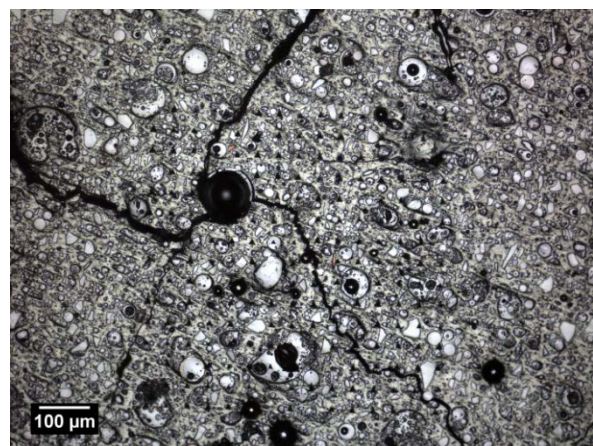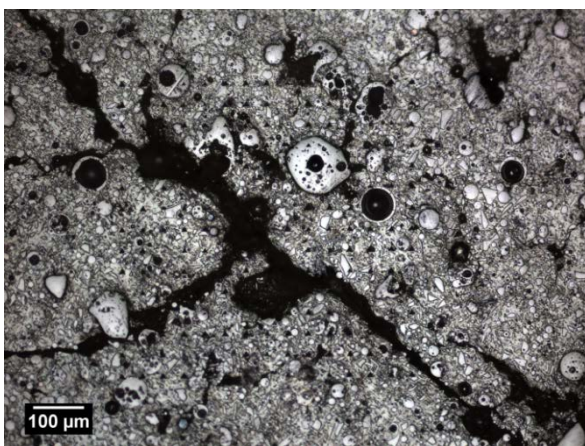slightly bright/white particles are partially reacted FA and GBFS particles.

Fig. 14a. Optical microscope photo of S50 sample in the natural laboratory conditions (left: edge) and (right: core).
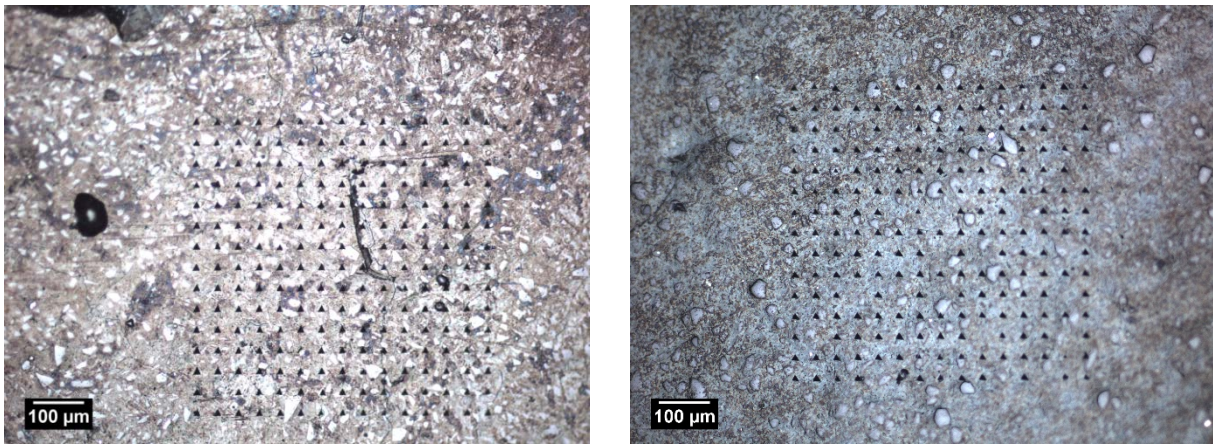

Fig. 14b. Optical microscope photo of S100 sample in the natural laboratory conditions (left: edge) and (right: core).

1   The intermixing of the phases can be expected during the measurements due to

2   inherent heterogenous nature of the studied material. However, the number of indents (200 in

3   this study) should be enough to represent E_m of the phases in the regions of interest. For

4   instance, Fig. 14b shows noncarbonated area of indents in the sample S100. It can be clearly

5   seen that the proportion of the indents printed on the rims between large GBFS particles and

6   the gel, is much less compared to the proportion of the indents printed solely in the gel. When

7   the effect of carbonation on the mechanical properties is tested in a standard way, such as

8   sample bulk testing of compressive strength of concrete [NEN 5988-1999], the error of

9   intermixing is far worse, since such a bulk analysis cannot separate the E_m values for different

10   phases in the system. The advantage of nanoindentation method is that E_m can be locally

11   tested, which otherwise could not be possible with other techniques. The possible error of

12   nanoindentation measurements regarding intermixing of the phases, is reduced by the number

13   of the measurements that were made for each of the areas of interest, noncarbonated and

14   carbonated. A representative SEM images of indents in noncarbonated area (blue triangles) in

15   sample S50 are shown in Fig. 15 (1, 2). In contrast, Fig. 15 (3, 4) show the carbonated areas

with a high degree of degradation occurs due to carbonation. The evolution of pores within the microstructure is visible in the vicinity of indents (red triangles) and overall surface. Fig. 16 shows a comparison between the results for E_m in the carbonated and noncarbonated indented areas in the form of a histogram. Every histogram represents approximately 200 indents from the sample.

In this study, four intervals of E_m were defined and linked to the E_m value of four features in the samples; (i) pores, $E_m<4$ GPa, (ii) carbonated C-(N-)A-S-H gel, $4<E_m<21$ GPa, (iii) noncarbonated C-(N-)A-S-H gel, $21<E_m<45$ GPa, (iv) unreacted FA and GBFS particles, $E_m>46$ GPa. The definition of the four intervals defined in this work is based on the results from the literature [25, 34, 59]. Ma [34] has reported E_m for different types of unreacted FA particles. The same FA type was used in this study as a precursor. The E_m of the Ca-rich FA particles was in the range of 75.7–91.2 GPa, the Fe-rich FA particles was 71.0–137.7 GPa, for Al-rich FA particles was between 33.3–65.4 GPa, and Si-rich FA particle presented the elastic modulus of 82.9 GPa. The E_m for GBFS particles and alkali-activated GBFS was found in the study of Puertas et al. [59]. Constantinides and Ulm reported the elastic modulus of C-S-H, and decalcified C-S-H, ranging between 19.5 and 31.8 GPa, 2.2 and 13.2 GPa, respectively [25].

Due to the uniform and dense microstructure, the E_m of the S100 sample was not altered under natural carbonation compared to the reference sample. Fig. 16 shows one range of the E_m for sample S100, which indicates its uniform phase composition. Unlike the mixture S100, the blended pastes were carbonated. The results were compared with those of equivalent noncarbonated parts of the samples, except for the paste S0. Due to low reactivity of FA in the S0 paste and consequently its low strength, the preparation of this sample for nanoindentation test was not possible.
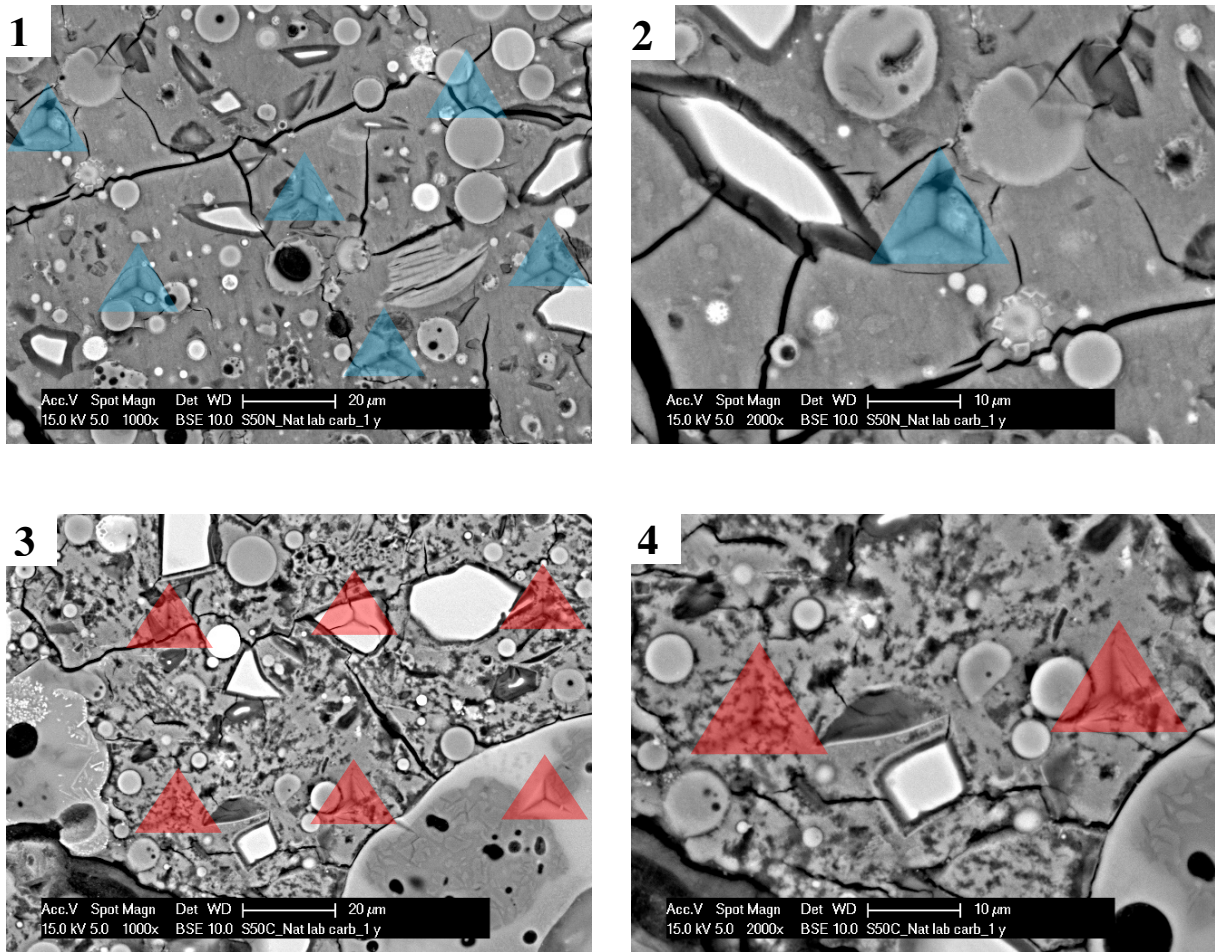
Fig. 15. Visualization of an indentation size for nanoindentation with respect to the noncarbonated (1, 2) and carbonated (3,4) microstructure morphology observed under the SEM.

1   The significant reduction of the E_m was identified in the carbonated pastes S30 and

2   S50, while the reduction of the E_m was of lower extent in paste S70. This can be explained by

3   the lower Ca content (Table 3) in S30 and S50 pastes which results in faster carbonation of

4   the reaction products in S30 and S50, compared to S70 or S100 pastes. On the other hand,

5   pastes S30 and S50 are more porous (Fig. 12, Table 6) compared to the paste S70 or S100,

6   and therefore faster CO_2 diffusion occurs in former. Carbonation mainly causes reduction of

7   the modulus of elasticity in the 5-45 GPa range, where values correspond to the E_m of the gel

8   (Fig. 16). These values shift to lower E_m values after carbonation, as found in the carbonated

9   blended OPC and GBFS cement paste by Çopuroğlu et al. [17]. Modification of the pore

1   structure due to the gel decalcification, is the main reason for E_m reduction, supported by MIP

2   and N_2 adsorption results which showed increase in pore sizes and BET surface area of the

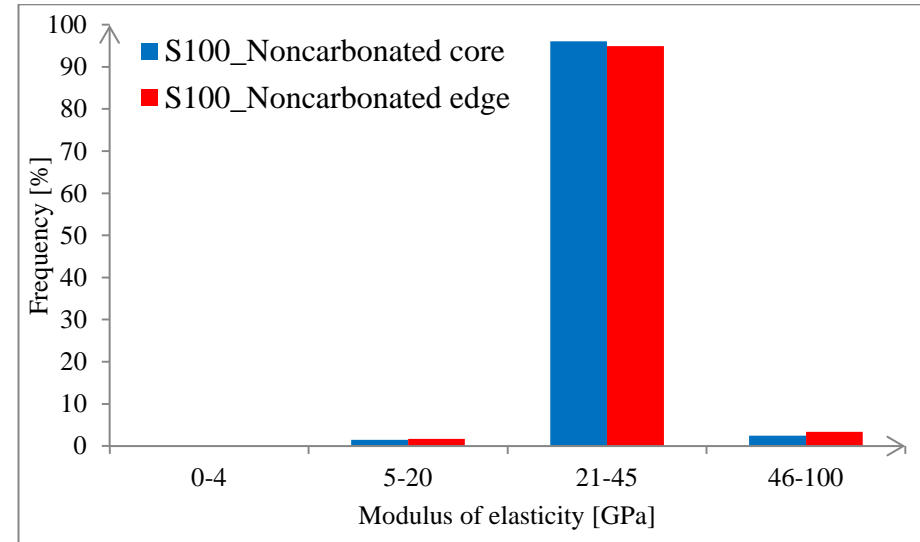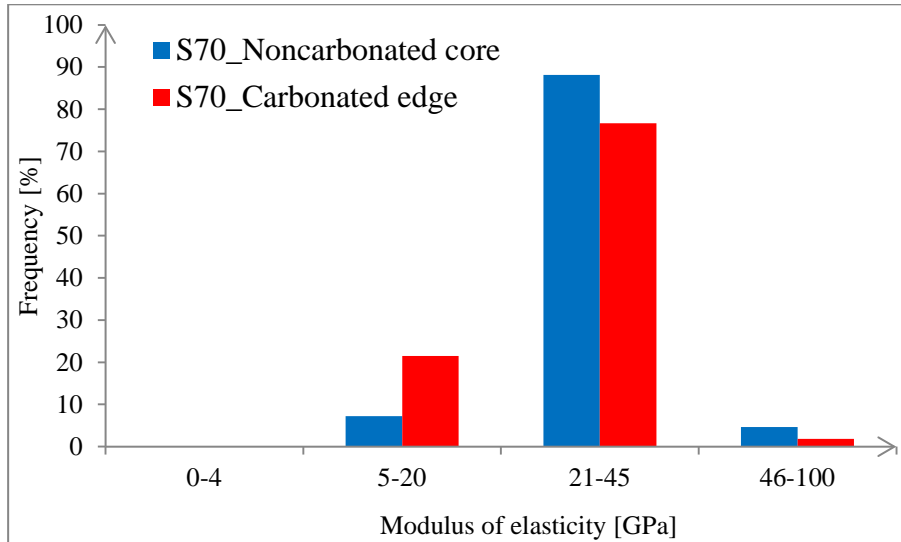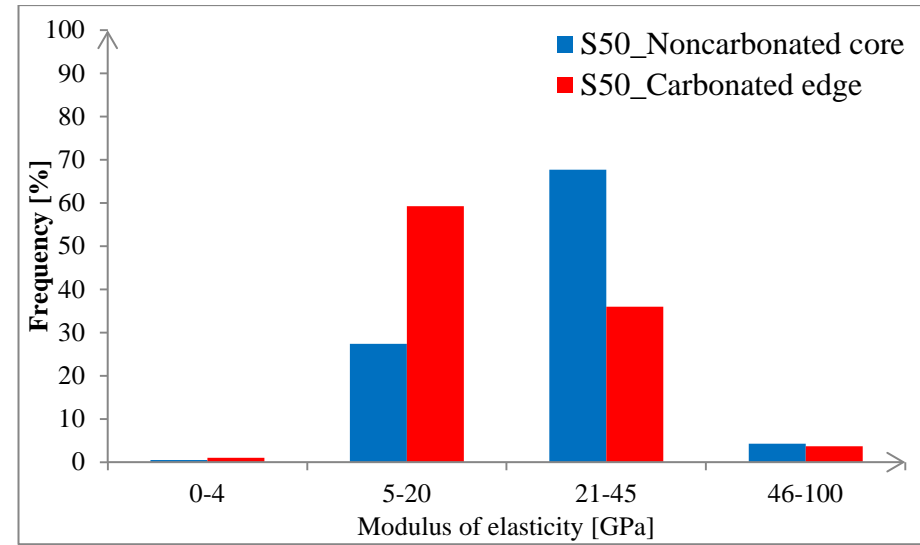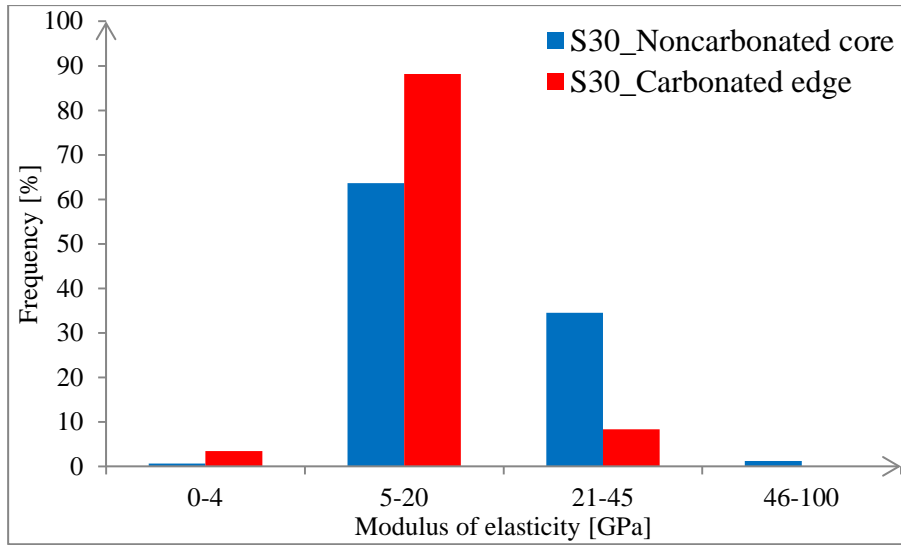3   carbonated samples compared to the noncarbonated (Table 6 and Table 7).

Fig. 16. Effect of natural carbonation on E_m.

4. Implications of natural carbonation in alkali-activated FA and GBFS pastes

The carbonation effects discussed in previous sections have important implications for the understanding of long-term performance in alkali-activated FA and GBFS pastes. In particular, chemical and physical assessments of the microstructure in the studied pastes were a prerequisite for understanding the change of their E_m due to natural laboratory carbonation. The natural laboratory carbonation of the five different paste mixtures resulted in different carbonation depths being governed by their composition and the pore structure in the samples. The results implied that limited carbonation in the GBFS-rich pastes might be a potential advantage in the extension of the service life of AAM. Improved testing of the complex pore structure may be needed for future predictive models.

The reference pastes S30, S50, S70 comprised mainly amorphous C-(N)-A-S-H gel, whilst the carbonated gel in these pastes was composed of calcium carbonates (vaterite and calcite) and silicates. Similar precipitation morphology is found in all blended alkali-activated pastes. Beside calcium carbonates precipitation such as showed by XRD, the polymerization of the silicate chains upon gel decalcification may cause a volumetric change, coarsening the pore structure. The range of the pores in noncarbonated gel (reference) is 0<r<50 nm, whereas gel after carbonation has larger pores, with 3<r<1000 nm. Since microstructure of the reference pastes has mainly gel pores, except S0 and S30 pastes (Fig. 12 and Fig. 13), the CO_2 molecules could not diffuse into the pastes S50, S70 and S100, considering that diffusion and transport of liquid and gas are mainly related to the capillary pores in the matrix. It is believed that the microcracks provided a diffusion of the CO_2 molecules and their dissolution in the pore liquid of the samples S50 and S70. The microcracks are most likely formed due to drying shrinkage considering their width and the depth as shown in the Fig. 17, after the samples were moved from the sealed curing conditions to the natural laboratory conditions. The observations of the microstructure under fluorescent light microscope separated denser

noncarbonated areas form the carbonated, degraded areas in the samples. The pastes emitted high (S0), normal (S30, S50), low (S70), and none (S100) fluorescence suggesting different densities in the noncarbonated and carbonated areas. The areas of the lower density (light green areas, Fig. 17) are where carbonation occurred and where E_m was reduced. It can be also seen that S70 sample has only been carbonated for a few mm along the outermost cracks. Fig. 17 also confirmed that no carbonation took place in the S100 paste.

Although the degradation due to carbonation in this study is investigated on a microscopic scale, the results give insight in large-scale systems such as concrete. The dominant structural failure of the OPC-based concrete due to carbonation, is mostly related to the corrosion of the steel reinforcement embedded in concrete rather than of the binder itself. Therefore, the transport properties of the hardened binder are essential in predicting the service life of structural OPC-based concrete. However, in AAM it is showed that carbonation might not be a cause of corrosion of the embedded steel reinforcement, since the pH in AAM, provided by the high concentrations of the alkali from the activators, can be kept above the value at which corrosion of the steel reinforcement in the concrete initiates, i.e. at the pH<9 [45]. Therefore, beside testing pH of the carbonated pore solution, and potential corrosion of steel reinforcement embedded in concrete as usually done in OPC-based materials, attention should be drawn to the degradation of the mechanical properties in carbonated AAM. Since the main reaction products in AAM are predominantly amorphous such as shown in this paper by XRD quantification measurements, the reduction of the E_m of the carbonated gel, might be a parameter that has to be considered in the predictive models for service life estimation in AAM due to carbonation effect. In addition, local evaluation of the degraded micromechanical properties of the paste is essential to explain the behaviour of concrete, whereas the change in carbonated paste-aggregate interface will have an additional effect.
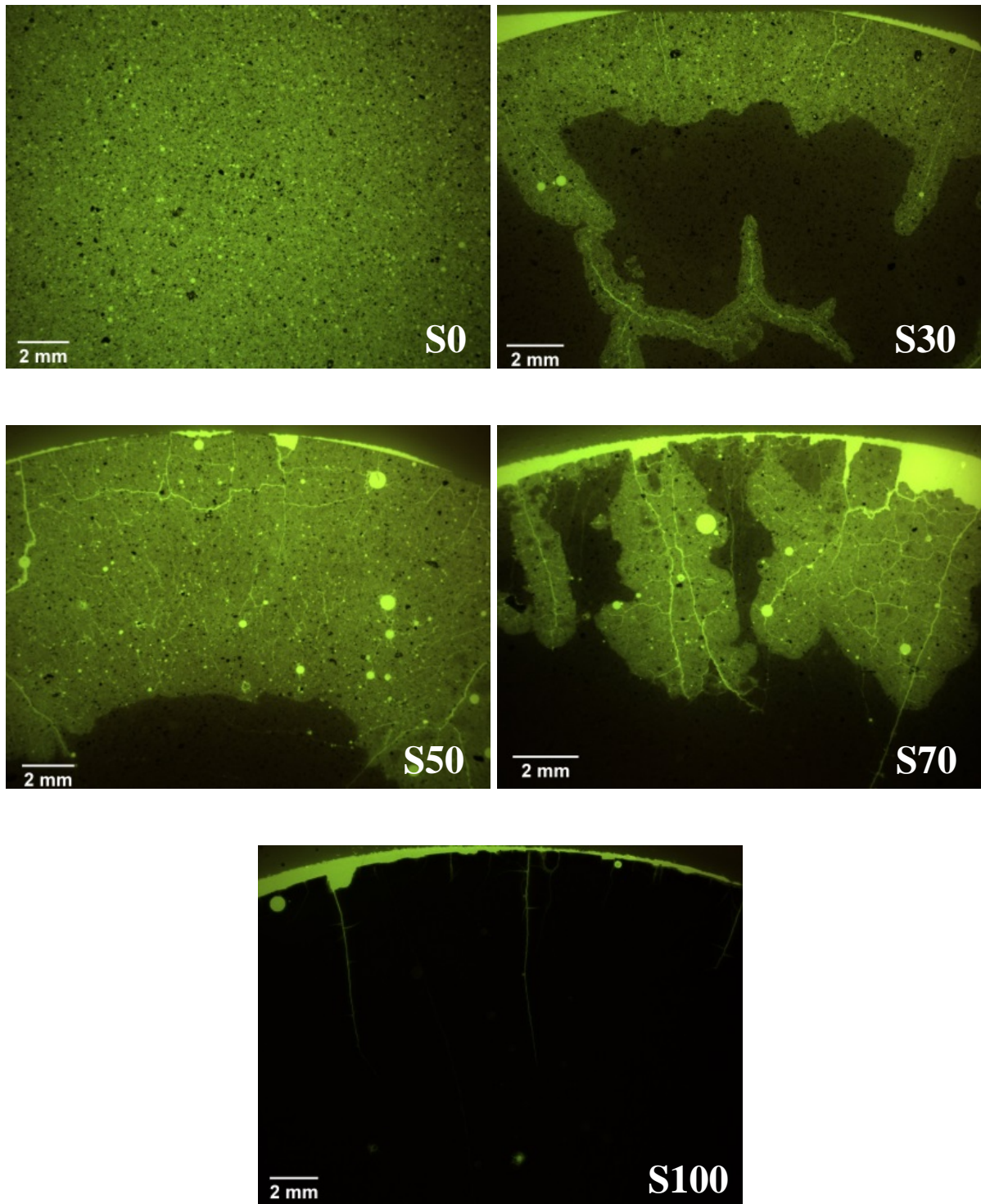
Fig. 17. Fluorescent yellow resin impregnated thin-section samples viewed in reflected fluorescent light, showing the carbonation depth from the top surface toward the core of the samples; noncarbonated matrix is dark grey to black; carbonated matrix, microcracks, voids and pores are light green.

5. Conclusions

The effect of carbonation on pore structure and E_m were studied in the alkali-activated FA and GBFS pastes after exposure in the natural laboratory conditions for 1 year. Results show that the alkali-activated FA (S0) except its pore solution has not carbonated in the studied conditions. Similarly, the alkali-activated GBFS (S100) was highly dense that CO_2 could not diffuse in the sample. N_2 adsorption tests identified the gel pores (with a pore diameter less than 10 nm) to be dominant in the noncarbonated pastes and this technique was more useful for pore structure characterization than the MIP method. The blended pastes were partially carbonated. The carbonation first led to the removal of Ca from the gel, forming vaterite and calcite. Subsequently, an excess of negative charges in the gel due to Ca removal, was balanced through formation of Si-OH or Si-O-Na groups. Condensation of neighbouring Si-OH or Si-O-Na groups into Si-O-Si formed silicate gel as found by ATR-FTIR analyses.

The main change in the pore size distribution occurred in the level of the nanometer pore sizes, whereas the significant increase of the surface area (BET) is identified in the carbonated S30, S50 and S70 pastes. The E_m decreased significantly in the carbonated samples S30 and S50 compared to the corresponding noncarbonated samples, whereas no significant change of the E_m was found in the pastes with 70 and 100 wt.% of GBFS. The potential advantage of using rich GBFS binders is seen in the extension of the service life of AAM.

References

1. J.S. van Deventer, J.L. Provis, P. Duxson, D.G. Brice, Chemical research and climate change as drivers in the commercial adoption of alkali activated materials, Waste Biomass Valorization. 1(1) (2010) 145-55.

2. J.S. van Deventer, J.L. Provis, P. Duxson, Technical and commercial progress in the adoption of geopolymer cement, Miner. Eng. 29 (2012) 89-104.

3. S.A. Bernal, E.D. Rodríguez, A.P. Kirchheim, J.L. Provis, Management and valorisation of wastes through use in producing alkali-activated cement materials, J. Chem. Technol. Biotechnol. 91(9) (2016) 2365-88.

4. F. Pacheco-Torgal, J. Labrincha, C. Leonelli, A. Palomo, P. Chindaprasit, Handbook of alkali-activated cements, mortars and concretes, Elsevier, 2014.

5. S.A. Bernal, J.L. Provis, Durability of Alkali-Activated Materials: Progress and Perspectives, J. Am. Ceram. Soc. 97(4) (2014) 997-1008.

6. K. Arbi K, M. Nedeljković, Y. Zuo, G. Ye, A review on the durability of alkali-activated fly ash/slag systems: advances, issues, and perspectives, Ind. Eng. Chem. Res. 55(19) (2016) 5439-53.

7. T. Bakharev, J.G. Sanjayan, Y.B. Cheng, Resistance of alkali-activated slag concrete to carbonation, Cem. Concr. Res. 31(9) (2001) 1277-83.

8. M. Palacios, F. Puertas, Effect of carbonation on alkali-activated slag paste, J. Am. Ceram. Soc. 89(10) (2006) 3211-21.

9. F. Puertas, M. Palacios, T. Vázquez, Carbonation process of alkali-activated slag mortars, J. Mater. Sci. 41(10) (2006) 3071-82.

10. S.A. Bernal, R.M. de Gutiérrez, A.L. Pedraza, J.L. Provis, E.D. Rodriguez, S. Delvasto, Effect of binder content on the performance of alkali-activated slag concretes, Cem. Concr. Res. 41(1) (2011) 1-8.

11. A. Morandeau, M. Thiery, P. Dangla, Investigation of the carbonation mechanism of CH and CSH in terms of kinetics, microstructure changes and moisture properties. Cem. Concr. Res. 56 (2014) 153-70.

12. R.J. Myers, S.A. Bernal, R. San Nicolas, J.L. Provis, Generalized structural description of calcium–sodium aluminosilicate hydrate gels: the cross-linked substituted tobermorite model, Langmuir. 29(17) (2013) 5294-306.

13. I. Soroka, Portland cement paste and concrete, 1980.

14. B. Šavija, M. Luković, Carbonation of cement paste: understanding, challenges, and opportunities, Constr. Build. Mater. 117 (2016) 285-301.

15. J. Han, G. Pan, W. Sun, C. Wang, D. Cui, Application of nanoindentation to investigate chemomechanical properties change of cement paste in the carbonation reaction, Science China Technological Sciences. 55(3) (2012) 616-22.

16. H.S. Shang, T.H. Yi, L.S. Yang. Experimental study on the compressive strength of big mobility concrete with nondestructive testing method, Adv. Mater. Sci. Eng. (2012)

17. O. Çopuroğlu, E. Schlangen, Modeling of frost salt scaling, Cem. Concr. Res. 38(1) (2008) 27-39.

18. J.J. Chen, Thomas JJ, H.M. Jennings, Decalcification shrinkage of cement paste. Cem. Concr. Res. 36(5) (2006) 801-9.

19. S.A. Bernal, R.M. de Gutierrez, J.L. Provis, V. Rose, Effect of silicate modulus and metakaolin incorporation on the carbonation of alkali silicate-activated slags. Cem. Concr. Res. 40(6) (2010) 898-907.

20. M. Nedeljkovic, Y.Zuo, K. Arbi, G. Ye, New test method for assessing the carbonation front in alkali-activated fly ash/slag pastes, in Non-Traditional Cement and Concrete VI. (2017) Brno, Czech Republic.

21. K. Scrivener, R. Snellings, B. Lothenbach, A practical guide to microstructural analysis of cementitious materials. (2016) CRC Press.

22. J. Kaufmann, Pore space analysis of cement-based materials by combined Nitrogen sorption-Wood's metal impregnation and multi-cycle mercury intrusion. Cem. Concr. Comp. 32(7) (2010) 514-522.

23. E.P. Barrett, L.G. Joyner, P.P. Halenda, The determination of pore volume and area distributions in porous substances. I. Computations from nitrogen isotherms. J. Am. Chem. Soc. 73(1) (1951) 373-80.

24. A.J. Katz, A.H. Thompson, Quantitative prediction of permeability in porous rock, Phys. Rev. B. 34(11) (1986) 8179.

25. G. Constantinides, F.J. Ulm, The effect of two types of CSH on the elasticity of cement-based materials: Results from nanoindentation and micromechanical modeling, Cem. Concr. Res. 34(1) (2004) 67-80.

26. O. Bernard, F.J. Ulm, E. Lemarchand, A multiscale micromechanics-hydration model for the early-age elastic properties of cement-based materials, Cem. Concr. Res. 33(9) (2003) 1293-309.

27. J.J. Hughes, P. Trtik, Micro-mechanical properties of cement paste measured by depth-sensing nanoindentation: a preliminary correlation of physical properties with phase type, Mater. Charact. 53(2) (2004) 223-31.

28. M. Luković, E. Schlangen E, G. Ye, Combined experimental and numerical study of fracture behaviour of cement paste at the microlevel, Cem. Concr. Res. 73 (2015) 123-35.

29. B. Šavija, M. Luković M, S.A. Hosseini, J. Pacheco, E. Schlangen, Corrosion induced cover cracking studied by X-ray computed tomography, nanoindentation, and energy dispersive X-ray spectrometry (EDS), Mater. Struct. 48(7) (2015) 2043-62.

30. I. Beleña, W. Zhu, Nanoindentation Study of Na-Geopolymers Exposed to High Temperatures, in Nanotechnology in Construction 3: Proceedings of the NICOM3, Z. Bittnar, et al., Editors. (2009), Springer Berlin Heidelberg: Berlin, 169-174.

31. J. Němeček, V. Šmilauer, L. Kopecký, Nanoindentation characteristics of alkali-activated aluminosilicate materials, Cem. Concr. Compos. 33(2) (2011) 163-70.

32. V. Šmilauer, P. Hlaváček, F. Škvára, R. Šulc, L. Kopecký, J. Němeček, Micromechanical multiscale model for alkali activation of fly ash and metakaolin. J. Mater. Sci. 46(20) (2011) 6545-55.

33. S. Das, P. Yang, S.S. Singh, J.C. Mertens, X. Xiao, N. Chawla, N. Neithalath, Effective properties of a fly ash geopolymer: Synergistic application of X-ray synchrotron tomography, nanoindentation, and homogenization models, Cem. Concr. Res. 78 (2015) 252-62.

34. Y. Ma, G. Ye, J. Hu, Micro-mechanical properties of alkali-activated fly ash evaluated by nanoindentation, Constr. Build. Mater. 147 (2017) 407-16.

35. F.J. Ulm, M. Vandamme, C. Bobko, J. Alberto Ortega, K. Tai, C. Ortiz, Statistical indentation techniques for hydrated nanocomposites: concrete, bone, and shale, J. Am. Ceram. Soc. 90(9) (2007) 2677-92.

36. W. Zhu, J.J. Hughes, N. Bicanic, C.J. Pearce, Nanoindentation mapping of mechanical properties of cement paste and natural rocks, Mater. Charact. 58(11) (2007) 1189-98.

37. F.J. Ulm, M. Vandamme, H.M. Jennings, J. Vanzo, M. Bentivegna, K.J. Krakowiak, G. Constantinides, C.P. Bobko, K.J. Van Vliet, Does microstructure matter for statistical nanoindentation techniques? Cem. Concr. Compos. 32(1) (2010) 92-9.

38. J.J. Chen, L. Sorelli, M. Vandamme, F.J. Ulm, G. Chanvillard, A Coupled Nanoindentation/SEM-EDS Study on Low Water/Cement Ratio Portland Cement Paste: Evidence for C–S–H/Ca(OH)$_2$ Nanocomposites, J. Am. Ceram. Soc. 93(5) (2010) 1484-93.

39. W.C. Oliver, G.M. Pharr, Measurement of hardness and elastic modulus by instrumented indentation: Advances in understanding and refinements to methodology, J. Mater. Res. 19(1) (2004) 3-20.

40. W.M. Jung, S.H. Kang, W.S. Kim, C.K. Choi, Particle morphology of calcium carbonate precipitated by gas-liquid reaction in a Couette-Taylor reactor. Chem. Eng. Sci. 55(4) (2000) 733-747.

41. C.Y. Tai, P.C Chen, Nucleation, agglomeration and crystal morphology of calcium carbonate. AIChE J. 41(1) (1995) 68-77.

42. D. Kralj, L. Brečević, A.E. Nielsen, Vaterite growth and dissolution in aqueous solution I. Kinetics of crystal growth. J. Cryst. Growth, 104(4) (1990) 793-800.

43. J. Hostomsky, A.G. Jones, Calcium carbonate crystallization, agglomeration and form during continuous precipitation from solution. J. Phys. D: Appl. Phys. 24(2) (1991) p.165.

44. Z. Šauman, Long-term carbonization of the phases $3CaO \cdot Al_2O_3 \cdot 6H_2O$ and $3CaO \cdot Al_2O_3 \cdot SiO_2 \cdot 4H_2$. Cem. Concr. Res. 2(4) (1972) 435-446.

45. S.A. Bernal, J.L. Provis, D.G. Brice, A. Kilcullen, P. Duxson, J.S. van Deventer, Accelerated carbonation testing of alkali-activated binders significantly underestimates service life: the role of pore solution chemistry. Cem. Concr. Res. 42(10) (2012) 1317-1326.

46. Hidalgo, A., Domingo, C., Garcia, C., Petit, S., Andrade, C. and Alonso, C., Microstructural changes induced in Portland cement-based materials due to natural and supercritical carbonation. J. Mater. Sci. 43(9) (2008) 3101-3111.

47. C.E. White, L.L. Daemen, M. Hartl, K. Page, Intrinsic differences in atomic ordering of calcium (alumino) silicate hydrates in conventional and alkali-activated cements. Cem. Concr. Res. 67 (2015) 66-73.

48. K. Sisomphon, O. Çopuroğlu, A.L. Fraaij, Development of blast furnace slag mixtures against frost salt attack, Cem. Concr. Compos. 32(8) (2010) 630-8.

49. C. Famy, K.L. Scrivener, A.K. Crumbie, What causes differences of CSH gel grey levels in backscattered electron images? Cem. Concr. Res. 32(9) (2002) 1465-71.

50. A.E. Morandeau, C.E. White, In situ X-ray pair distribution function analysis of accelerated carbonation of a synthetic calcium–silicate–hydrate gel. J. Mater. Chem. A 3(16) (2015) 8597-8605.

51. S.A. Bernal, J.L.Provis, B. Walkley, R. San Nicolas, J.D. Gehman, D.G. Brice, A.R. Kilcullen, P. Duxson, J.S. van Deventer, Gel nanostructure in alkali-activated binders based on slag and fly ash, and effects of accelerated carbonation. Cem. Concr. Res. 53 (2013) 127-44.

52. M. Nedeljkovic, K. Arbi, Y. Zuo, G. Ye, Physical properties and pore solution analysis of alkali-activated fly ash-slag pastes. In: 2016 Proceedings pro113: International RILEM Conference Materials Systems and Structures in Civil Engineering 2016 (MSSCE 2016), Denmark

53. M.B. Haha, B. Lothenbach, G.L. Le Saout, F. Winnefeld, Influence of slag chemistry on the hydration of alkali-activated blast-furnace slag-Part I: Effect of MgO. Cem. Concr. Res. 41(9) (2011) 955-963.

54. N.J. Clayden, S. Esposito, A. Aronne, P. Pernice, Solid state ^{27}Al NMR and FTIR study of lanthanum aluminosilicate glasses, J. Non-Cryst. Solids. 258(1) (1999) 11-9.

55. A. Fernández-Jiménez, A. Palomo, Mid-infrared spectroscopic studies of alkali-activated fly ash structure, Microporous and mesoporous materials, 86(1) (2005) 207-14.

56. P. Yu, R.J. Kirkpatrick, B. Poe, P.F. McMillan, X. Cong, Structure of calcium silicate hydrate (C-S-H): Near-, Mid-, and Far-infrared spectroscopy, J. Am. Ceram. Soc. 82(3) (1999) 742-8.

57. D. Dimas, I. Giannopoulou, D. Panias, Polymerization in sodium silicate solutions: a fundamental process in geopolymerization technology. J. Mater. Sci. 44(14) (2009) 3719-3730.

58. G. Ye, Experimental study and numerical simulation of the development of the microstructure and permeability of cementitious materials, Ph.D. thesis, Delft University of Technology, The Netherlands, 2003.

59. F. Puertas, M. Palacios, H. Manzano, J.S. Dolado, A. Rico, J. Rodríguez. A model for the CASH gel formed in alkali-activated slag cements, J. Eur. Ceram. Soc. 31(12) (2011) 2043-56.